Nitrate transboundary heavy pollution over East Asia in winter

Syuichi Itahashi[1], Itsushi Uno[2], Kazuo Osada[3], Yusuke Kamiguchi[3#], Shigekazu Yamamoto[4], Kei Tamura[5], Zhe Wang[2,6], Yasunori Kurosaki[6], Yugo Kanaya[7]

[1] Environmental Science Research Laboratory, Central Research Institute of Electric Power Industry, 1646 Abiko, Abiko, Chiba, 270-1194, Japan
[2] Research Institute for Applied Mechanics, Kyushu University, 6-1 Kasuga Park, Kasuga, Fukuoka, 816-8580, Japan
[3] Graduate School of Environmental Studies, Nagoya University, D2-1 (510) Furo-cho, Chikusa-ku, Nagoya, Aichi, 464-8601, Japan
[4] Fukuoka Institute of Health and Environmental Sciences, 39 Mukaizano, Dazaifu, Fukuoka, 818-0135, Japan
[5] Nagasaki Prefectural Environmental Affairs Department, 2-1306-11 Ikeda, Omura, Nagasaki, 856-0026, Japan
[6] Institute of Atmospheric Physics, Chinese Academy of Sciences, 40 Huayanli, Chaoyang, Beijing, 100029, China
[7] Arid Land Research Center, Tottori University, 1390 Hamasaka, Tottori, 680-0001, Japan
[8] Japan Agency for Marine-Earth Science and Technology, 3173-25 Showa-machi, Kanazawa-ku, Yokohama, Kanagawa, 236-0001, Japan
[#]Present address: JCB Co. Ltd., Tokai Regional Office, 2-16-26, Nishiki, Naka-ku, Nagoya, Aichi 460-0003, Japan

Correspondence to: Syuichi Itahashi (isyuichi@criepi.denken.or.jp)

Abstract. High $PM_{2.5}$ concentrations reaching around 100 $\mu g/m^3$ were observed twice during an intensive observation campaign in January 2015 at Fukuoka (33.52°N, 130.47°E) in western Japan. These events were analyzed comprehensively by a regional chemical transport model and synergetic ground-based observations with state-of-the-art measurement systems, which can capture the behavior of secondary inorganic aerosols (SO_4^{2-}, NO_3^-, and NH_4^+). The first episode was dominated by NO_3^- (type N), whereas the second episode was dominated by SO_4^{2-} (type S). The concentration of NH_4^+, which is the counterion for SO_4^{2-} and NO_3^-, was high for both types. The sensitivity simulation of the chemical transport model showed that the dominant contribution was from transboundary air pollution for both types. To investigate the differences between these types of transboundary heavy pollution further, the chemical transport model results were examined in combination with the backward trajectory analysis. For both types, high concentrations of NO_3^- above China were found, and the air mass that originated from northeast China reached Fukuoka, but the traveling time from the coastline of China to Fukuoka was 18 h for type N and 24 h for type S. The conversion ratio of SO_2 to SO_4^{2-} (Fs) was less than 0.1 for type N, but reached 0.3 for type S as the air mass approached Fukuoka. The higher Fs for type S was related to the higher relative humidity and concentration of HO_2, which produces the most effective oxidant, H_2O_2, for the aqueous-phase production of SO_4^{2-}. Analyzing the gas ratio, which is an indicator of the sensitivity of NO_3^- to changes in SO_4^{2-} and NH_4^+, showed that the air mass over China was super NH_3-rich for type N, but was almost NH_3-neutral for type S. Thus, although the high concentration of NO_3^- above China gradually decreased during transport from China to Fukuoka, higher NO_3^- concentrations were maintained during transport owing to the lower SO_4^{2-} for type N, whereas the production of SO_4^{2-} led to decomposition of NH_4NO_3 and more SO_4^{2-} was transported for type S. It is also noteworthy that the type N transport pattern was limited to

western Japan, especially over Kyushu island. The transboundary air pollution dominated by SO_4^{2-} (type S) has been recognized as major pattern over East Asia. However, our study confirms the importance of the transboundary air pollution dominated by NO_3^- (type N), which will help refine our understanding of the transboundary heavy $PM_{2.5}$ pollution in winter over East Asia.

1 Introduction

Particulate matter (PM) presents major environmental problems globally, especially in East Asia. A typical example is the episode of severe air pollution that occurred in January 2013 above China (e.g., Wang et al., 2014; Uno et al., 2014). During this episode, PM with aerodynamic diameters of less than 2.5 μm ($PM_{2.5}$) reached record-breaking concentrations of 772 μg/m^3 on January 12, 2013 (Pan Y. al., 2016). The transboundary air pollution in downwind regions resulting from the severe air pollution in China is also an important environmental problem. For example, the possible long-range transport of $PM_{2.5}$ was based on the comparison of observations in metropolitan areas and remote islands in western Japan (Kaneyasu et al., 2014). They highlighted the dominant effect of the transboundary transport for sulfate (SO_4^{2-}) as a major $PM_{2.5}$ component in western Japan throughout most of the year. During spring, due to the prevailing westerly wind over East Asia, transboundary air pollution of both aerosols and gases (e.g., carbon monoxide (CO) and ozone (O_3)) have been discussed thoroughly (Itahashi et al., 2010; 2013; 2015; Kanaya et al., 2016; Nagashima et al., 2010). In summer, the clean air mass from oceans is moved over Japan by the southerly wind caused by the Pacific High; however, some studies have discussed the importance of transboundary air pollution from China over western Japan (Itahashi et al., 2012a; Ikeda et al., 2014). Recently, one-year source-receptor relationships for SO_4^{2-} were evaluated, and China was identified as the main influence on downwind regions throughout the year, with local sulfur dioxide (SO_2) emissions making an important contribution during summer (Itahashi et al., 2016). Compared with the analyses for spring and summer, transboundary air pollution events during winter are less well understood.

In this study, we also focused on nitrate (NO_3^-), which is an important $PM_{2.5}$ component. NO_3^- in $PM_{2.5}$ is produced via the reaction of gas-phase nitrate (nitric acid; HNO_3) and ammonia (NH_3), and this process is reversible. This reaction favors a shift toward the aerosol phase at low temperatures and high humidity (Seinfeld and Pandis, 2006). The simulated spatial distribution over East Asia showed the possible impact of the transboundary pollution of NO_3^- during winter over western Japan (Zhang et al., 2007; Ying, 2014). However, a quantitative evaluation over downwind regions was not presented in their studies. This is partly because model ability was not evaluated owing to the difficulty in measuring NO_3^-. Particulate NH_4NO_3 may be volatilized after collection on the filter, by either an increase in the pressure drop across the particle-collecting medium or changes in the gas-aerosol equilibrium during sampling (Sickles et al. 1999; Chang et al., 2000). This volatilization could occur even in winter because the temperature in the instrument shelter can be increased by heat from the pump. Therefore, the ground-based Acid Deposition Monitoring Network in East Asia uses the four-stage filter pack method: NH_4NO_3 is collected on the first filter and gas-phase HNO_3 and NH_3 are detected on the subsequent filters. The

artifacts might not be significant; however, to avoid the possibility of volatilization, total nitrate (the sum of NO_3^- and HNO_3) has been used to evaluate the model ability in previous studies (e.g., Kajino et al., 2011).

To improve our understanding of the behavior of NO_3^-, accurate measurements and the evaluation of model ability are needed. In this study, we used the state-of-the-art automated monitoring system for SO_4^{2-} and NO_3^-, Aerosol Chemical Speciation Analyzer (ACSA). This system measures SO_4^{2-} and NO_3^- with high temporal resolution and 1 h intervals were used in this study, minimizing the possibility of volatilization. In addition, the behavior of ammonium (NH_4^+), which is the counterion for SO_4^{2-} and NO_3^-, was captured by the well-validated NHx monitoring system. Therefore, the secondary inorganic aerosols (sulfate (SO_4^{2-})−nitrate (NO_3^-)−ammonium (NH_4^+); SNA) were fully observed by our synergetic monitoring system. The denuder-filter pack (D-F pack) method with 6-8 h cycles was also used during the intensive observation period from January 7–17, 2015. This intensive observation was designed to capture the heavy $PM_{2.5}$ pollution episode in winter time, and to support and validate the ACSA and NHx monitoring system. Based on these measurement systems, gas-phase HNO_3 and NH_3 can be measured by the D-F pack method and NHx monitor, respectively. The related gas-phase behavior analysis is valuable for improving our understanding of the formation of NO_3^-. The observations were conducted at the Chikushi Campus of Kyushu University, which is in the suburbs of Fukuoka City (33.52°N, 130.47°E) in western Japan. The synergetic ground-based observation dataset was systematically interpreted by using the regional chemical transport model, and we also examined the impact of the domestic and transboundary air pollution during winter. Chemical transport model studies are one type of critical approach for analyzing the behavior of three-dimensional air pollutants and estimating source impacts. Systematic comparison of model results with observations, including gas-phase precursors, will promote understanding and improve model ability for Asia. This will also contribute to the Model Inter-Comparison Study for Asia (MICS-Asia), which focuses on providing a common understanding of model performances and uncertainties, especially for models of long-range transport in Asia (Carmichael et al., 2002; 2008, Li et al., 2017). This paper is constructed as follows. Section 2 documents the observation dataset and model simulation. Section 3 discusses the results with respect to temporal variations at observation sites and the model results combined with the backward trajectory analysis. Finally, a summary and conclusions are given in Section 4.

2 Observation and model simulation

2.1 Observation sites

The synergetic observations for capturing SNA behavior were conducted at Chikushi Campus of Kyushu University located in the suburbs of Fukuoka City (33.52°N, 130.47°E). Fukuoka City is the largest center of commerce in Kyushu Island. The population of Fukuoka City is 1.5 million and that of the Fukuoka metropolitan area is 2.5 million. This is the fourth largest metropolitan area in Japan, after Tokyo (34.8 million), Osaka (12.2 million), and Nagoya (5.5 million). This site is an urban site. In addition to the observation at Fukuoka, observations from the Goto Islands (32.68°N, 128.83°E) and Tsushima Island (32.20°N, 129.28°E) were also used. The Goto Islands are located in the East China Sea, 190 km southwest of Fukuoka, and

they have a population of 70,000. Tsushima Island is located in the Tsushima straits, 140 km northwest of Fukuoka, and has a population of 34,000. These two islands have negligible anthropogenic emissions sources and are regarded as remote sites. In addition to these three sites over Kyushu island, to investigate the regions affected by transboundary air pollution, observations from Tottori City (35.54°N, 134.21°E) in western Japan were also used. Tottori City has a population of 190,000, and this site is also regarded as a remote site in western Japan. The locations of these four observation sites over Japan are shown in Fig. 1. In addition to these observations over Japan, $PM_{2.5}$ observations in China from the US Embassy in Beijing and the US Consulates in the provincial capitals of Shanghai and Shenyang were used. The locations of these three sites over China are shown in Fig. 2.

2.1.1 Aerosol chemical speciation analyzer (ACSA)

An ACSA-12 Monitor (Kimoto Electric Co., Ltd., Osaka, Japan), for PM_{10} and $PM_{2.5}$, which were separated by a US Environmental Protection Agency inlet and a virtual impactor, were measured with high temporal resolution (Kimoto et al., 2013). PM was collected on a tape filter made of Teflon (PTFE). Hourly observations were conducted for SO_4^{2-} and NO_3^- at Fukuoka. The mass concentrations of PM were determined by using the beta-ray absorption method. The ACSA-12 measured NO_3^- using an ultraviolet spectrophotometric method, and SO_4^{2-} by turbidimetry after addition of $BaCl_2$ to form $BaSO_4$ and polyvinyl pyrrolidone as a stabilizer. The analytical period was within 2 h of sampling; therefore, the volatilization of particulate NH_4NO_3 after collection was regarded as small compared with the traditional filter-pack observation method. ACSA has been tested (Osada et al., 2016) and used to analyze the severe winter haze in Beijing (Zheng et al., 2015; Li et al., 2016), and to identify the aerosol chemical compositions at Fukuoka (Pan X. et al., 2016)

2.1.2 NHx monitor

The behaviors of NH_3 and NH_4^+ are also important because they are the counterions for SO_4^{2-} and NO_3^-. The concentrations of gaseous NH_3 and aerosol NH_4^+ were measured with a semi-continuous microflow analytical system (Kimoto Electric Co. Ltd., MF-NH$_3$A, Osada et al., 2011) at Fukuoka. The atmospheric NHx was dissolved in ultrapure water with a continuous air–water droplet sampler and quantified by fluorescence (excitation, 360 nm; emission, 420 nm) of the *o*-phtalaldehyde–sulfite–NH_3 reaction product (Genfa et al., 1989). Two inlet lines were used to differentiate the total amounts of NHx and particulate NH_4^+ after gaseous NH_3 was removed by a phosphoric acid-coated denuder from the sample air stream. The cut-off diameter of the inlet impactor was about 2 μm.

2.1.3 Denuder-filter pack method (D-F pack)

During the intensive observation period from January 7–17, 2015, D-F pack measurements were conducted at Fukuoka to validate the ACSA and NHx monitoring measurement systems. An annular denuder–multi-stage filter sampling system was used for HNO_3 and size-segregated aerosol sampling. The sampling interval was 6–8 h. At the inlet, coarse-mode aerosols were removed by Nuclepore membrane filters (111114, Nomura Micro Science Co., Ltd., Atsugi, Japan, pore size: 8 μm),

and then gas-phase HNO_3 was collected with the annular denuder (2000-30x242-3CSS, URG Co.) coated with NaCl (Perrino et al., 1990). Fine-mode aerosols were collected with a PTFE filter (J100A047A, ADVANTEC, Tokyo, Japan, pore size: 1 μm), and a nylon filter (66509, Pall Co.) captured volatized NO_3^- from the PTFE filter (Appel et al., 1981; Vecchi et al., 2009). Because of the use of an annular denuder system before PTFE filter collection, the adsorption of HNO_3, which would otherwise lead to overestimation of NO_3^- was low. The sample air flow rate was 16.7 L/min (1 atm, 25 °C). Under these conditions, the aerodynamic diameter of 50% cut-off for the Nuclepore filter was about 1.9 μm (John et al., 1983). The samples were analyzed by ion chromatography (IC). Comparing size-segregated SO_4^{2-} and NO_3^- data based on the D-F pack method with that from ACSA showed systematic differences. Linear regression analysis of fine-mode and coarse-mode SO_4^{2-} and NO_3^- showed good correlation, but the slope was not unity. Fine-mode aerosols were underestimated by the D-F pack relative to ACSA measurements, and coarse-mode aerosols were overestimated by the D-F pack relative to ACSA measurements. However, by summing the fine- and coarse-mode data, the slope between D-F pack and ACSA results was close to unity. The difference in the cut-off diameter of the D-F pack method was considered to be the most important factor in explaining differences between results from D-F pack and ACSA. More details of the comparison and validation of ACSA data are reported in Osada et al. (2016).

2.1.4 PM-712

Hourly PM_{10} and $PM_{2.5}$ concentrations were measured by a PM monitor (PM-712, Kimoto Electric Co., Ltd.) at the Goto Islands, Tsushima Island, and Tottori. PM-712 used the beta ray attenuation method to measure the mass concentrations of PM_{10} and $PM_{2.5}$. The ionic constituents of the species on the PTFE tape filters were also analyzed by IC to compare the aerosol behavior at Fukuoka and the other sites. At all sites, sample spots collected on the tape filter were covered with polyester tape to avoid contamination and crosstalk interference during storage. The sampling duration for the PM-712 tape filters was 1 h, except for Tottori where it was 3 h. For chemical analysis, four consecutive 1 h tape samples were combined into one sample for the Goto Islands and Tsushima Island. For Tottori, tape samples for 1 or 0.5 days were combined. Because of a temperature change during PM sample storage, some NO_3^- may have escaped via volatilization of HNO_3 from the sample. Therefore, NO_3^- data from the Goto Islands, Tsushima Island, and Tottori were not used. NH_4^+ are also affected by the volatilization in the case of it formed NH_4NO_3, but it forms $(NH_4)_2SO_4$ in preference. The data of NH_4^+ was used to indicate the concentration trapped by SO_4^{2-}. Hereafter, we call these datasets from the PM tape samples 'tape filter'.

2.1.5 Beta attenuation monitors

Hourly $PM_{2.5}$ concentrations in China were measured by beta attenuation monitors (BAMs) (1020, MetOne Instruments, Inc., Grants Pass, OR, USA) at the U.S. Embassy in Beijing from April 8, 2008, at the U.S. Consulates in Shanghai from December 21, 2011, and at the U.S. Consulates in Shenyang from April 22, 2013 (MOE, 2016). In the BAM technique, PM is collected on a quartz filter tape over a given time interval and the attenuation of beta rays through the sample is measured

and correlated directly with the PM mass. The details and the statistical analysis results of the BAM observation at the U.S. Embassy and Consulates are found in the work of San Martini et al. (2015).

2.1.6 Multi-angle absorption photometer (MAAP)

Observations of black carbon (BC), a primary aerosol that directly reflects local emissions contributions, from Fukuoka and the Goto Islands were also used to distinguish domestic and transboundary air pollution. BC is observed by using a multi-angle absorption photometer (MAAP; MAAP5012, Thermo Fisher Scientific, Waltham, MA, USA) (Petzold et al., 2005). In this method, the absorbance of the particles deposited on the filter is distinguished from scattering by reflectance measurements at multiple angles and by transmittance. This is to minimize the effects of coexisting aerosol particles other than BC on filter-based absorption photometers. The comparison measurements of BC from the Goto Islands were previously performed by Kanaya et al. (2013), and they reported that the BC MAAP measurements were strongly correlated with measurements by other techniques but had a positive bias. From the results reported by Kanaya et al. (2013), the MAAP absorption cross section of 6.6 m^2/g was systematically increased to 10.3 m^2/g at 639 nm. There were no MAAP BC measurements from the Goto Islands before January 11, 2015 during the intensive observation period.

2.2 Chemical transport model

The chemical transport model simulation was performed by using the Community Multi-scale Air Quality (CMAQ) modeling system version 4.7.1 (Byun and Schere, 2006) with nesting over East Asia. The meteorological fields of CMAQ were prepared with the Weather Research and Forecasting model version 3.3.1 (Skamarock et al., 2008) with analysis nudging applied to the National Centers for Environmental Prediction final operational global analysis data. The model domain covers the whole of East Asia with an 81 km horizontal grid resolution, with a 95 × 75 grid centered at 30°N and 115°E on a Lambert conformal projection. The nested domain covers eastern China and the whole of Japan with a 27 km horizontal grid resolution and a 145 × 145 grid. The vertical grid for sigma-pressure coordinates extends to 50 hPa with 37 layers with nonuniform spacing. The lateral boundary condition was as given by the global chemical transport model of Geos-Chem (Uno et al., 2014). The simulation period was from January 1–17, 2015, and the first 6 days were discarded as model spin-up time. The dry deposition velocity of HNO_3 over land was increased by a factor of five based on the model intercomparison results (Shimadera et al., 2014; Morino et al., 2015).

Emissions were set as follows. Anthropogenic emissions and natural sources of NOx from soil were obtained from the latest Regional Emission inventory in ASia (REAS) version 2.1 (Kurokawa et al., 2013), which covers 2000 to 2008. Therefore, the emissions for January 2008 were used in this study. This assumption is based on the following reasons. Satellite observation of the NO_2 column showed a decreasing trend in NOx emissions from China of -6%/year after 2011, and the levels for 2015 are similar to those for 2009 (Irie et al., 2016). In contrast, the NO_2 column over Japan decreased until 2013, and then began to increase from 2013 owing to the change in power plant use after the Fukushima Daiichi nuclear disaster (Morino et al., 2011). The level of the NO_2 column over Japan in 2015 was close to that in 2008 (Irie et al., 2016). The

installation of flue-gas desulfurization systems in power plants in China decreased SO_2 emissions in China from 2005 to 2006; after this turning point, SO_2 emissions generally showed a decreasing trend but the variation in SO_2 emissions is complicated (Xia et al., 2016). The assumption about the 2008 level for SO_2 emissions may overestimate the actual status. In Japan, SO_2 emissions are increasing for the same reasons as for NOx; however, there are no reliable references for the

5   current status of SO_2 emissions. Considering these factors in the variation of NOx and SO_2 emissions over China and Japan, it was assumed that the 2008 emissions would be within the range of uncertainty of the bottom-up emission inventories. Because REAS does not consider the monthly variation in NH_3, we used the monthly variation estimated by Huang et al. (2013). Annual NH_3 emission amount was also adjusted to match the estimate of Huang et al. (2013). Other anthropogenic emissions, such as BC, organic carbon (OC), and volatile organic compounds (VOC), were also assumed to be at the 2008

10   level due to the lack of information needed to update the status. The anthropogenic emission amounts of SO_2, NOx, and NH_3 on January 2015 are listed in Table 1. Biogenic emissions were prepared from MEGAN (Model of Emissions of Gases and Aerosols from Nature) (Guenther et al., 2012). As a biogenic source, dimethylsulfide (DMS) was not treated in the modeling system. Biomass burning emissions were used from the climatological database of RETRO (REanalysis of the TROpospheric chemical composition) (Schulrz et al., 2008). Volcanic activity data were taken from ACESS (Ace-Asia and

15   TRACE-P Modeling and Emission Support System) (Streets et al., 2003) and were modified by the volcanic activity observation data from the Japan Meteorological Agency (JMA) for available volcanoes (JMA, 2016). Fourteen main active volcanoes in Japan and Mt. Mayon and Mt. Bulsan on Luzon Island in the Philippines were considered. The model simulation using the above dataset is referred to as the base case simulation. The modeling system domain with overlaid anthropogenic NOx emissions is shown in Fig. 3.

20   To investigate whether the effect of domestic or transboundary air pollution is dominant, we also conducted a sensitivity simulation, in which the anthropogenic emissions in Japan are switched off. Here, anthropogenic emissions were taken from the REAS inventory; because of this, emissions from agriculture were included. Shipping emissions were not treated in the sensitivity simulation. In terms of O_3, which is involved in complex nonlinear chemistry, larger nonlinearities in the atmospheric concentration response to emissions variation for China but not Japan were clarified due to the higher amount of

25   emissions from China than from Japan (Itahashi et al., 2015). Therefore, the sensitivity simulation was designed to remove anthropogenic emissions in Japan instead of those in China. Based on the differences between the base case simulation and this sensitivity simulation, the domestic contribution from Japan was estimated.

3 Results and Discussion

3.1 Meteorological conditions

30   Meteorological conditions during the intensive observation campaign from January 7–17, 2015 are shown in Fig. 4 with observations and model results. Meteorological observation stations of the JMA in the corresponding nested model grid of Fukuoka were used. Temperatures (Fig. 4a) were around 5 °C at night and 10 °C during the day in January 2015. On January

9, the temperature was nearly 0 °C at Fukuoka. For the wind field (Fig. 4b and c), because of the dominance of the northwesterly wind system from the Asian continent during winter, the wind direction was generally 270°–360° (west to north) and the wind speed was around 5 m/s, with the exception of January 9 and 12–15. On January 9, when the coldest temperature during the intensive observation campaign was observed, the wind speed was less than 1 m/s and wind direction was from the south. On January 13–15, the wind speed was also low, at 2–3 m/s, and the wind direction was easterly, caused by a warm front passing over the south of Kyushu Island on January 14. After the warm front had passed, the relative humidity was close to 100% on January 15–16 (Fig. 4d), with a maximum of 10 mm/h rain on January 15 (Fig. 4e). The model tended to underestimate the precipitation amount, as we have reported in a previous study (Itahashi et al., 2014). Comparing the observations with the model results shows that our modeling system generally captures the observed meteorological variations during this episode.

3.2 Temporal variation of particulate matter

(a) $PM_{2.5}$

The temporal variation of $PM_{2.5}$ over Japan at Fukuoka, Tsushima Island, the Goto Islands, and Tottori are presented in Fig. 1. $PM_{2.5}$ observation data are taken from ACSA at Fukuoka, and are taken from PM-712 at other sites. Temporal resolutions are 1 h for all observations. During the analyzed period of January 7–17, 2015, episodic $PM_{2.5}$ peaks reached around 100 μg/m^3 at Fukuoka twice. The first peak, observed at 12:00 LT on January 11 (shown in blue in Fig. 1) reached a maximum concentration of 86.4 μg/m^3 at Fukuoka and 105.1 μg/m^3 at the Goto Islands. During this first peak, the concentration at Tsushima Island was 63.9 μg/m^3, which was lower than at the other remote island site in the Goto Islands, and there was no distinctive peak at Tottori. The second peak observed at 00:00 LT on January 17 (shown in red in Fig. 1) reached a maximum concentration at Fukuoka of 106.2 μg/m^3. During this second peak, the remote sites of the Goto Islands and Tsushima Island also recorded high $PM_{2.5}$ concentrations of 104.8 and 89.1 μg/m^3, respectively, and the $PM_{2.5}$ concentration reached 37.6 μg/m^3 at Tottori. In Fig. 1, we show the model results as black lines. Generally, the model captured the observed temporal $PM_{2.5}$ behavior, although it underestimated the first peaks at Fukuoka and the Goto Islands, and the second peak at the Goto Islands. The timing of the high $PM_{2.5}$ concentration was reproduced well by the modeling system. Statistical analysis of the model reproducibility demonstrated that all paired datasets for $PM_{2.5}$ showed good correlations between the observations and the model at the four sites in Japan, with a correlation coefficient (R) of 0.86. Mean fractional bias (MFB) and mean fractional error (MFE) were -42.6% and 67.4%, respectively, and these results satisfied the model performance criteria (MFB ≤ ±60% and MFE ≤ +75%) proposed by Boylan and Russell (2006). Figure 1 also shows the model results of a sensitivity simulation performed by switching off the Japanese anthropogenic emissions. The sensitivity simulations results are shown as dotted black lines and the difference between the base case and the sensitivity simulation is shown in gray, which indicates the domestic contribution of Japan. Except for Fukuoka, there were little domestic contributions for $PM_{2.5}$; therefore, the transboundary air pollution was dominant during January 2015 at remote sites in western Japan. At Fukuoka, although domestic contributions for $PM_{2.5}$ were found in some cases on January 8–10 and 14,

the concentration of $PM_{2.5}$ was lower compared with the two peaks. During the two episodes when $PM_{2.5}$ concentration reached around 100 μg/m^3 over Japan, the model simulation suggested that the effect of transboundary air pollution was dominant, even at Fukuoka.

The temporal variations of $PM_{2.5}$ over China at Beijing, Shanghai, and Shenyang are shown in Fig. 2. $PM_{2.5}$ observation data are taken from BAM-1020 and the temporal resolution is 1 h. At Beijing, there were high concentrations of $PM_{2.5}$ which correspond to the high concentration of $PM_{2.5}$ found over Japan. One high concentration was approximately 300 μg/m^3 on January 10–11, and other was around 600 μg/m^3 on January 16. These peak times were almost one day before the high concentration was observed over Japan. At Shanghai, there were two clear peaks with a $PM_{2.5}$ concentration of 200 μg/m^3 on January 11 and 17. The time corresponded well with the peak time over Japan. At Shenyang, where the local emissions from domestic sources were dominant in winter, the temporal variation was complex compared with Beijing and Shanghai. $PM_{2.5}$ showed sharp peaks several times with concentrations of around 300 μg/m^3, whereas the model only showed gentle peaks. Analysis of the model reproducibility showed that all $PM_{2.5}$ paired datasets for the observations and model at three sites over China showed that R was 0.73, and MFB and MFE were -9.8% and 46.8%, respectively; satisfying the model goal criteria (MFB ≤ ±30% and MFE ≤ ±50%) proposed by Boylan and Russell (2006). The evaluation of model performance over China supports the discussion of downwind regions.

(b) SNA

The temporal variations of SNA are shown in Figs. 5 and 6. In Fig. 5, SO_4^{2-} and NH_4^+ are shown for four sites in Japan. At Fukuoka, ACSA and D-F pack observations are shown for SO_4^{2-}, and NHx monitor and D-F pack results are shown for NH_4^+. The temporal resolutions of ACSA and the NHx monitor were 1 h, and those of the D-F packs were 6–8 h depending on the samples. For the Goto Islands, Tsushima Island, and Tottori, the PM-712 tape filter data were used. The temporal resolution was 4 h at the Goto Islands and Tsushima Island, and 1 or 0.5 day at Tottori. In Fig. 6, NO_3^-, HNO_3, NH_3, and total ammonia (sum of NH_4^+ and NH_3) are shown for Fukuoka. ACSA and D-F pack observations for NO_3^- are shown, D-F pack observations are shown for HNO_3, and NHx monitor observations are shown for NH_3 and total ammonia. Because of a temperature change during PM-712 sample storage, NO_3^- concentrations could have been affected by volatilization; hence, only NO_3^- analysis at the Fukuoka site was used. At Fukuoka, the SNA concentration contributed 52% and 46% of the $PM_{2.5}$ concentration in the first and second episodes, respectively. For SO_4^{2-} (Fig. 5 (left)), the concentration during the second episode was larger than during the first episode at Fukuoka, the Goto Islands, and Tsushima Island. At Tottori, there was no peak for the first episode for SO_4^{2-}. In contrast to SO_4^{2-}, a higher NO_3^- concentration was observed during the first episode instead of the second episode (Fig. 6). NH_4^+ showed high concentrations during both episodes because it is the counterion for SO_4^{2-} and NO_3^- (Fig. 5 (right)). Based on the analysis of the $PM_{2.5}$ (Fig. 3) and SNA (Figs. 5 and 6) observations, the $PM_{2.5}$ concentrations were similar during the episodes on January 11 and 17; however, the main component of SNA was NO_3^- during the first episode and SO_4^{2-} during the second episode. At Fukuoka, the relative portions of SO_4^{2-}, NO_3^-, and NH_4^+ within $PM_{2.5}$ were respectively 18%, 20%, and 14% during the first episode, and 27%, 6%, and 14% during the second

episode. Therefore, the first episode (shown in blue in Figs. 3, 5, and 6) is referred to as 'type N', and the second episode (shown in red in Figs. 3, 5, and 6) is referred to as 'type S' hereafter.

The model results for the base case and sensitivity simulations are overlaid with the same temporal resolution as the observations in Figs. 5 and 6. The model tended to underestimate the SO_4^{2-} concentration (Fig. 5 (left)); however, the model reproduced the features of types N and S, and sensitivity simulation indicated the dominance of transboundary air pollution for SO_4^{2-} during the intensive observation campaign in January 2015, even at Fukuoka. For NO_3^- (Fig. 6), the model reproduced the features of the type N and S peaks well, although the model overestimated the dip in NO_3^- concentration found from the evening of January 10 to before the type N episode. The D-F pack observations generally underestimated NO_3^- compared with the ACSA observations, because of the difference in cut-off diameter between these measurement systems. Except for the type N and S episodes, domestic contributions were seen for NO_3^- on January 8–10 and 14. However, the sensitivity simulation confirmed that the transboundary NO_3^- air pollution was dominant for types N and S. Because NH_4^+ is the counterion for both SO_4^{2-} and NO_3^-, small domestic contributions for NH_4^+ were observed at Fukuoka (Fig. 5 (right)). This result corresponded to the domestic contribution for NO_3^-. For the other three remote sites, there were no domestic contributions for NH_4^+.

The behavior of SNA, gas-phase HNO_3, and NH_3 were analyzed comprehensively based on the NHx monitor and D-F pack observations (Fig. 6) to support our understanding of NO_3^- behavior. There are few synergetic analyses including gas-phase behavior over the downwind region of Asian continent. Peaks for gas-phase HNO_3 were found for types N and S, whereas the concentration of gas-phase NH_3 was nearly zero (less than 1 μg/m^3 for 24 h average) for types N and S, and on January 8, 10, 12, and 15 (green arrows in Fig. 6). Type S, in particular, showed almost zero concentration of NH_3. The concentration of total ammonia showed distinct peaks for types N and S; therefore, the nearly zero concentration of NH_3 suggested the full conversion of NH_3 to produce NH_4^+ as a counterion for SO_4^{2-} and NO_3^-. The sensitivity simulation, in which Japanese anthropogenic emissions were switched off, clarified the different features of related gas-phase species. The base case simulation and sensitivity simulation were similar for HNO_3, suggesting it originated from transboundary air pollution. A slight increase in HNO_3 in the sensitivity simulation was found on January 8–10 and 12 (red arrows in Fig. 6). These were the complex cases connected to overseas and domestic emissions. If there are no Japanese NH_3 emissions, the transported HNO_3 cannot produce NO_3^- in Japan, and so it remains as gas-phase HNO_3. The synergetic analysis for gas-phase HNO_3 and NH_3 indicated that abundant HNO_3 was transported from abroad and reacted with domestic NH_3, producing NO_3^- on January 8–10. Compared with these cases, domestic HNO_3 and NH_3 produced NO_3^- on January 14 (orange arrows in Fig. 6). The concentrations were lower than for type N and S, which were dominated by the transboundary air pollution.

(c) Coarse mode aerosols

Coarse-mode aerosols were also partly analyzed in this study. Because of the effect of transboundary air pollution on HNO_3 (Fig. 6), we focused on coarse-mode NO_3^-. Coarse-mode NO_3^- is produced by reactions of HNO_3 with mineral dust or sea-salt particles. In general, mineral dust mainly has an effect in spring over East Asia (Itahashi et al., 2010), whereas sea-salt

particles play an important role throughout the year. Recently, we reported the importance of coarse-mode NO_3^- as an atmospheric input in East Asian ocean regions (Itahashi et al., 2016). Figure 7 shows the modeled and observed coarse-mode NO_3^-, Na^+, and Cl^-. ACSA and D-F pack observations are shown for coarse-mode NO_3^-, and D-F pack observations are shown for coarse-mode Na^+ and Cl^-. During the intensive observation period in January, coarse-mode NO_3^- also showed high

5 concentrations for types N and S of around 10 μg/m^3, and on January 9–10 of around 5 μg/m^3. Based on the model results, because the domestic contribution for HNO_3 was found on January 14 (Fig. 6), the domestic contribution for coarse-mode NO_3^- was found only on January 14, but the concentration was below 1 μg/m^3. Na^+ and Cl^- from sea-salt particles also had peaks for types N and S. Sea-salt particles are mechanically produced by high winds; therefore, these peaks generally corresponded to high wind speeds (Fig. 2). High winds were observed on January 15, and Na^+ and Cl^- peaks occurred, but

10 the coarse-mode NO_3^- concentration was close to zero. This was because there was no HNO_3 to react with NaCl from January 12–15, and wet deposition of coarse-mode NO_3^- with precipitation from noon on January 14 to the evening of January 15. For coarse-mode NO_3^-, transboundary air pollution was the dominant factor. This means that a large amount of HNO_3 was transported from abroad (Fig. 5) and reacted with sea-salt particles over the ocean, and reached Fukuoka in the air mass.

(d) BC

To support the discussion of the domestic and the transboundary contributions to SNA, the behavior of BC at Fukuoka and the Goto Islands are shown in Fig. 8. The sensitivity simulation would suffer from a nonlinear chemistry response if complex atmospheric chemistry were involved; hence, we focused on BC, which is a primary aerosol. The temporal variation of BC

20 also showed distinctive peaks for types N and S at Fukuoka and the Goto Islands. The model results reproduced these peaks well, and the sensitivity simulation also suggested the dominance of transboundary air pollution for both peaks N and S. The temporal variation at the Goto Islands showed only two peaks of types N and S, although many short-term peaks were seen at Fukuoka. The sensitivity simulation confirmed that domestic air pollution contributed to these short-term peaks at Fukuoka; however, the model could not fully capture the peaks observed on January 7, 13, and 14. To improve the

25 performance of the model to capture these short-term peaks, a higher-resolution model simulation and a revision of the emission inventory are needed. Analysis of the primary aerosol confirmed that the transboundary air pollution was dominant for types N and S in January 2015.

Consequently, the well-validated model simulation indicated that two high $PM_{2.5}$ episodes with concentrations of around 100 μg/m^3 that occurred over western Japan during January were dominated by NO_3^- for the first peak (type N) and by SO_4^{2-} for

30 the second peak (type S), and that NH_4^+ concentration was high for both types. The model sensitivity simulation clarified that these high SNA concentrations in the type N and S episodes were dominated by the transboundary air pollution. In addition to the transport of SNA, abundant gas-phase HNO_3 and coarse-mode NO_3^- reacted with sea-salt particles over the ocean and were also transported to western Japan. NH_3, which mainly came from domestic emissions, showed concentrations around zero during type N and S events, suggesting that NH_3 was depleted to neutralize SO_4^{2-} and NO_3^-.

3.2 Trajectory analysis

Analyzing the synergetic observations at Fukuoka and the other three remote sites in Japan with the regional chemical transport model demonstrated that the two $PM_{2.5}$ episodic peaks were dominated by transboundary heavy pollution, even at Fukuoka. The two peaks had different SNA compositions. The first episode on January 11 showed a high NO_3^- (type N) concentration and the second episode on January 17 was dominated by SO_4^{2-} (type S). The differences in these episodes were investigated further by a model simulation combined with backward trajectory analysis. The spatial distributions of SO_4^{2-} and NO_3^- during type N and S patterns are shown in Figs. 9 and 10, respectively.

In type N (Fig. 9 (right)), the model results showed that a low SO_4^{2-} concentration of less than 5 μg/m^3 and a high NO_3^- concentration of more than 10 μg/m^3 covered Fukuoka. The spatial distribution patterns indicated the outflow of SO_4^{2-} and NO_3^- from continental Asia to western Japan. The dominance of the transboundary air pollution suggested by these spatial distributions was consistent with the model sensitivity simulation results (Figs. 5 and 6). High-concentration regions of SO_4^{2-} and NO_3^- stretched from the eastern coastline of China to the East China Sea and western Japan. The spatial distribution implied the direct transport from continental Asia to the downwind regions. In addition, the high-concentration region stretched from eastern China to western Japan, consistent with the corresponding $PM_{2.5}$ peak on January 11 at Shanghai and over Japan. To investigate the air mass origin for type N, the HYSPLIT backward trajectory (Stein et al., 2015) starting from Fukuoka over 72 h was analyzed (T_N in Fig. 9 (right)). The backward trajectory during type N transport suggested that the air mass originated from Shaanxi province and passed over Shanxi province, southern Hebei province, Shandong province, and then reached Fukuoka. The traveling time from the coast of China to Fukuoka was about 18 h. The distance from the coastline of China to Fukuoka is approximately 1000 km, so the air mass speed for type N was 55.6 km/h. Fig. 9 (left) shows the spatial distribution for when the air mass was located over China. A high concentration of NO_3^- of more than 60 μg/m^3 occurred over the east coast of China before the air mass arrived in Fukuoka, whereas the SO_4^{2-} concentration was as high as 10 μg/m^3 above the East China Sea.

In type S (Fig. 10 (right)), the model calculated that a high SO_4^{2-} concentration of more than 20 μg/m^3 and a low NO_3^- concentration of around 5 μg/m^3 covered Fukuoka. The HYSPLIT backward trajectory is shown as T_S in Fig. 10. The air mass during type S transport originated from Shanxi province and slowly moved over northern Henan province, Shandong province, and reached Fukuoka within about 24 h. The high-concentration regions stretched from eastern China to western Japan, consistent with the simultaneous $PM_{2.5}$ peak at Shanghai and over Japan. The air mass was stagnant over China compared with type N transport. The spatial distribution when the air mass was located over China is shown in Fig. 10 (left). For SO_4^{2-}, the concentration was higher when the air mass arrived at Fukuoka compared with that in China, suggesting the fast production of SO_4^{2-} during the transport process. A high concentration of SO_4^{2-} of 20 μg/m^3 spread over the East China Sea and western Japan. A high NO_3^- concentration of more than 60 μg/m^3 occurred over China, similar to type N; however, the NO_3^- concentration was immediately reduced during the transport. The high NO_3^- concentration of more than 10 μg/m^3 did not reach Fukuoka in this type S transport. Comparing the spatial distribution of the air mass over Fukuoka (Fig. 10

(right)) and China (Fig. 10 (left)) showed a 1 day delay in the high concentration peaks over Japan compared with the peak for Beijing (Figs. 3 and 4).

The backward trajectories for types N and S both showed similar transport patterns from China and Fukuoka. However, the spatial distribution patterns demonstrated clear differences between SO_4^{2-} and NO_3^- distributions for type N and S patterns. To discuss the different mechanisms for type N and S further, the model results were analyzed along the backward trajectories of T_N and T_S. The path analyses are shown in Figs. 11 and 12, along with additional indexes. The conversion ratio of SNA from the gas- to aerosol-phases is an important indicator. For SO_4^{2-}, considering the concentration of their gas-phase species of SO_2, the conversion ratio of Fs is defined as follows and calculated based on molar concentrations, shown in square brackets (Khoder, 2002).

$$F_s = \frac{[SO_4^{2-}]}{[SO_2] + [SO_4^{2-}]} \quad [mol/mol]. \quad (1)$$

A ratio of 0 indicates that SO_4^{2-} was not produced, and a ratio of 1 indicates that SO_2 was converted completely to SO_4^{2-}. To confirm the Fs analysis, the concentration of the highly reactive hydroperoxy radical (HO_2) was also analyzed. Self-reaction of HO_2 produces hydrogen peroxide (H_2O_2), and this is the most effective oxidant of aqueous-phase SO_2 (Pandis and Seinfeld, 1989). Because the analyzed period was during winter, aqueous-phase reactions would be the main pathway for producing SO_4^{2-}.

For NO_3^-, the conversion ratios of Fn are defined by considering the concentration of NO_2 as a precursor and calculated based on molar concentrations (Khoder, 2002).

$$F_n = \frac{[HNO_3] + [NO_3^-]}{[NO_2] + [HNO_3] + [NO_3^-]} \quad [mol/mol]. \quad (2)$$

To investigate the ratio of NO_3^- to gas- and aerosol-phase components, analogous to the calculation for SO_4^{2-}, the conversion ratio of Fn' is introduced.

$$F_n' = \frac{[NO_3^-]}{[HNO_3] + [NO_3^-]} \quad [mol/mol]. \quad (3)$$

The behavior of SNA is determined by introducing candidate indicators according to the work of Ansari and Pandis (1998) and Pinder et al. (2008). The gas ratio (GR) is an indicator of the sensitivity of NO_3^- to changes in SO_4^{2-} and NH_4^+ concentration. The GR is defined as the ratio of free ammonia to total nitrate as

$$GR = \frac{[NH_3 + NH_4^+] - 2[SO_4^{2-}]}{[HNO_3 + NO_3^-]} \quad [mol/mol], \quad (4)$$

where it is assumed that SO_4^{2-} is fully neutralized, as indicated by the coefficient of 2 for $[SO_4^{2-}]$. The GR value implies the following condition for NO_3^- production.

$$\begin{cases} \text{GR} > 1: \text{NH}_3 - \text{rich} \\ 0 < \text{GR} < 1: \text{NH}_3 - \text{neutral} \\ \text{GR} < 0: \text{NH}_3 - \text{poor} \end{cases} \quad (5)$$

Here, NH_3-rich means that there is sufficient NH_3 to neutralize both SO_4^{2-} and NO_3^-, NH_3-neutral means that there is sufficient NH_3 to neutralize SO_4^{2-}, and NH_3-poor means that there is insufficient NH_3 to neutralize SO_4^{2-} or NO_3^-. Free ammonia, which can form NH_4NO_3 in the equilibrium process, is quantified more accurately by adjusting $[\text{SO}_4^{2-}]$ with the degree of sulfate neutralization (DSN). The DSN is defined as

$$\text{DSN} = \frac{[\text{NH}_4^+] - [\text{NO}_3^-]}{[\text{SO}_4^{2-}]} \quad [\text{mol/mol}], \quad (6)$$

where DSN is equal to or greater than 2 if there is sufficient NH_4^+. By substituting the coefficient of 2 before $[\text{SO}_4^{2-}]$ in Eq. (2) with Eq. (4), the adjusted GR (adjGR) can be defined as

$$\text{adjGR} = \frac{[\text{NH}_3 + \text{NH}_4^+] - \text{DSN} \times [\text{SO}_4^{2-}]}{[\text{HNO}_3 + \text{NO}_3^-]} = \frac{[\text{NH}_3] + [\text{NO}_3^-]}{[\text{HNO}_3] + [\text{NO}_3^-]} \quad [\text{mol/mol}], \quad (7)$$

by using the indexes, and the path analysis of backward trajectories for the model results are shown in Figs. 11 and 12, and are summarized in Table 1. The analyses are shown for (a) the meteorological components of temperature and relative humidity, (b) SO_4^{2-} and SO_2 with an enlarged view for SO_4^{2-}, (c) HO_2 concentration, (d) NO_3^-, HNO_3, NO, NO_2, other NOy consisting of NO_3, HNO_2, N_2O_5, and peroxyacyl nitrates (PANs), and coarse-mode NO_3^-, (e) NH_4^+ and NH_3, and (f) adjGR, Fs, and Fn'. The concentrations of the air pollutants were reduced by chemical reactions, dispersion, and deposition during the transport; therefore, as an index of dispersion and deposition processes, BC and CO concentrations normalized to their maximum concentrations during the transport were used in the variation of the total concentration in (b), (d), and (e). Table 1 shows the meteorological components and the air pollutant concentrations of each component and total sulfate, total nitrate, and total ammonia. The indexes were averaged over China, the transport time above the ocean, and Fukuoka. The SNA concentration was balanced between SO_4^{2-} with NO_3^- and NH_4^+ during both types N and S.

During the type N pattern (Fig. 11), the concentration of air pollutants increased after the air mass moved into Hebei province (-30 h). The relative humidity was lower than 40% when the air mass traveled over Shanxi and Hebei provinces (Fig. 11a). The SO_4^{2-} concentration was around 1 μg-S/m^3 during transport (Fig. 11b and Table 1), and SO_2 was dominant in the total sulfate concentration. In this type N pattern, the concentration of the most effective oxidant of HO_2 for the SO_2 aqueous-phase reaction was smaller due to the lower relative humidity (Fig. 11c), and the conversion ratio was less than 0.1 (Fig. 11f and Table 1). Compared with the SO_4^{2-} variation, as the trajectory passed from Shanxi province (-36 h) to Shandong province (-18 h), and over the ocean (-12 h), NO_3^- and NH_4^+ concentration increased. The concentration of NO_3^- and NH_4^+ decreased as the air mass traveled to Japan (Figs. 11d and 11e). Over China (-30 to -18 h), gas-phase NH_3 was abundant and HNO_3 was fully consumed to produce NH_4NO_3 (Figs. 11d and 11e). The excess HNO_3 over the ocean contributed to producing coarse-mode NO_3^- by reacting with sea-salt particles as the air mass traveled over the ocean (Fig. 11d). The adjGR was super NH_3-rich over China (Fig. 11f). After the air mass left Shandong, HNO_3 increased and NH_3 was

close to zero (Figs. 11d and 11e), so adjGR shifted to NH_3-neutral status (Fig. 11f). Consequently, the proportion of NO_3^-, indicated by Fn', remained around 80% during transport from China to Japan (Fig. 11f). The rate of the decrease of total sulfate, total nitrate, and total ammonia were generally consistent with the rate of decrease of normalized BC and CO, suggesting that the budget was almost satisfied during transport (Table 1). The decrease of BC was larger than that of CO

5   because of wet deposition (e.g., Pan et al., 2011, Kanaya et al., 2016).

During the type S pattern (Fig. 12), SNA concentrations were higher compared with the type N pattern (Fig. 11), partly due to the slower motion of the air mass compared with type N. SO_4^{2-} concentration was around 2 µg-S/m^3 over Shanxi to Henan provinces (-72 to -36 h), it increased slightly to 3 µg-S/m^3 over Henan to Shandong provinces (-36 to -24 h), and subsequently increased to 3 µg-S/m^3 over the ocean (Fig. 12b and Table 1). The aqueous-phase reaction contributed to the

10   production, as suggested by the variation in HO_2 concentration. Over oceans, the relative humidity was around 80%, 20% larger than in the case of the type N pattern (Fig. 12a and Table 1). The Fs conversion ratio was 0.3 when the air mass reached Fukuoka (Fig. 12f). The increase in SO_4^{2-} over Fukuoka compared with over China was +67.2% (Table 1). The behaviors of gas-phase HNO_3 and NH_3 were similar in type N patterns (Figs. 12d and 12e); the NH_3 concentration was high over China, and HNO_3 gradually increased after the air mass approached the ocean, partly because coarse-mode NO_3^- was

15   produced. However, the NH_3 concentration was smaller compared with type N patterns and remained near zero when the air mass passed over Henan province (Fig. 12e). adjGR showed slight NH_3-rich status over China (-54 to -36 h), and shifted to NH_3-neutral status before the air mass left China (-36 h), and at the same time, the ratio of NO_3^- indicated by Fn' decreased to 0.45 (Fig. 12f and Table 1). Similar to type N, the rates of decrease of total sulfate, total nitrate, and total ammonia were generally consistent with the rates of decrease of normalized BC and CO.

20   To summarize the key points for type N and S patterns, the behavior of SO_4^{2-}, NO_3^-, and HNO_3 concentrations during transport from China to Japan are shown in Fig. 13. The relative percentages of the concentration of each species to the total concentration of SO_4^{2-}, NO_3^-, and HNO_3 are shown. It is clear that NO_3^- was not produced, whereas SO_4^{2-} was produced during transport from China to Fukuoka. Types N and S both showed the dominance of NH_4NO_3 (over 70%) when the air mass was over China (-48 h). For the air mass close to Fukuoka, because there was no NH_3, NH_4NO_3 decomposed into gas-

25   phase NH_3 and HNO_3. Therefore, HNO_3 concentration increased as the air mass reached Fukuoka for types N and S. At this time, the SO_4^{2-} concentration was important in determining the NO_3^- concentration. SO_4^{2-} production (Figs. 11b and 12b) through an aqueous-phase reaction was indicated by the HO_2 concentration (Figs. 11c and 12c), and Fs showed a large difference between types N (lower than 0.1 during transport; Figs. 11f) and S (around 0.3 at Fukuoka; Figs. 12f). Once H_2SO_4 was produced via an aqueous-phase reaction, it reacted with gas-phase NH_3 to produce $(NH_4)_2SO_4$, leading to further

30   decomposition of NH_4NO_3. The ratio of NO_3^- (Fn') showed different behavior for types N (around 0.8 during transport; Figs. 11f) and S (lower than 0.5 at Fukuoka; Figs. 12f). The transport pattern under similar conditions over China was determined by the low SO_4^{2-} concentration maintaining a higher NO_3^- concentration at Fukuoka (type N), or by SO_4^{2-} production under a higher relative humidity resulting in the dominance of SO_4^{2-} with further NH_4NO_3 decomposition (type S).

3.3 Outflow analysis

Finally, the outflow of SO_4^{2-} and NO_3^- from China to western Japan during the intensive observation campaign is summarized in Fig. 14. In this figure, the modeled SO_4^{2-} and NO_3^- concentrations were averaged at 32–36°N to cover the four sites in Japan (Fig. 3) and are shown as a time-longitude cross section. The longitude of Shanghai, the Goto Islands, Tsushima Island, Fukuoka, and Tottori are indicated at the bottom of the figure. This outflow analysis can help to identify the areas affected by transboundary heavy pollution. The main outflow from China to western Japan occurred twice (types N and S). The outflow concentration of SO_4^{2-} was lower on January 11 for type N and larger on January 17 for type S; a high concentration of more than 15 μg/m^3 reached 130°N (Fukuoka) and a concentration of around 10 μg/m^3 reached 134°N (Tottori) for type S (Fig. 14a). The outflow of NO_3^- was observed over the Goto Islands, Tsushima Island, and Fukuoka on January 11 for type N, whereas the high concentration of over 10 μg/m^3 was limited to the East China Sea regions on January 17 for type S. A concentration of NO_3^- of more than 5 μg/m^3 did not reach 134°N (Tottori) for type N (Fig. 14b). The outflow analysis suggested that SO_4^{2-} can be transported longer distances, whereas transboundary air pollution of NO_3^- is limited to western Japan, especially over Kyushu.

4 Conclusion

Based on the state-of-the-art observation systems for capturing SNA behavior and the chemical transport model, two episodes of high $PM_{2.5}$ concentrations of around 100 μg/m^3 occurred during winter over western Japan were analyzed. The first episode on January 11 was dominated by NO_3^- (type N) and the second episode on January 17 was dominated by SO_4^{2-} (type S). The chemical transport model captured the behavior of SNA and the related gas-phase species of HNO_3 and NH_3, and coarse-mode NO_3^- observed over Japan. The model also reproduced $PM_{2.5}$ variation over China. To evaluate the domestic contributions, sensitivity analysis was performed, in which the anthropogenic emissions from Japan were switched off in the chemical transport model. The results showed that there were sometimes domestic contributions for NO_3^-, although the type N and S patterns were dominated by the transboundary air pollution, even at Fukuoka. The effect of transboundary air pollution on type N and S patterns were also confirmed by analyzing the behavior of BC at Fukuoka and the remote Goto Islands. The importance of the transboundary air pollution for coarse-mode NO_3^-, produced by abundant HNO_3 and sea-salt particles, was also revealed. To investigate the characteristic differences between type N and S patterns, the chemical transport model results were analyzed by the backward trajectory analysis from Fukuoka to continental Asia. We also evaluated the adjusted gas ratio (adjGR), which indicates the sensitivity of NO_3^- to changes in SO_4^{2-} and NH_4^+, and Fs, which is the conversion ratio of SO_2 to SO_4^{2-}. For the SO_2 aqueous-phase reaction, H_2O_2 is the most effective oxidant. Thus, HO_2, which produces H_2O_2 through self-reaction, was also analyzed. The features of type N and S patterns are summarized as follows.

- In the type N transport pattern, NO_3^- was mainly the NH_4^+ counterion during transport from China to Japan. A high NO_3^- concentration of more than 10 μg/m^3 was observed at Fukuoka. NH_3 was abundant and HNO_3 was completely

consumed to produce NO_3^- over China; hence adjGR indicated super NH_3-rich status, which meant full neutralization of both SO_4^{2-} and NO_3^-, over China. After the air mass left China, HNO_3 increased and NH_3 was close to zero; so adjGR shifted to NH_3-neutral status. The SO_4^{2-} concentration was always lower than the NO_3^- concentration. This was because the HO_2 concentration was less than 3 pptv during transport from China to Fukuoka, and Fs suggested a slow conversion ratio for SO_4^{2-} of less 0.1. SO_4^{2-} production via an aqueous-phase reaction was also inhibited. This also explained why the air mass maintained a higher NO_3^- concentration during transport.

- In the type S transport pattern, the ion balance between NH_4^+ and NO_3^- with SO_4^{2-} showed that the counterion of NH_4^+ was mainly NO_3^- over China, and then became SO_4^{2-} as the air mass left China and approached Fukuoka. A high concentration of SO_4^{2-} of more than 20 μg/m^3 was observed at Fukuoka. The change in Fs from 0.1 to 0.3 when the air mass reached Fukuoka was consistent with this observation. Higher Fs values were related to higher relative humidity and HO_2 concentration, indicating the high production of SO_4^{2-} via an aqueous-phase reaction (H_2SO_4). The production of H_2SO_4 promoted the reaction with NH_3 to produce $(NH_4)_2SO_4$ and further decomposition of NH_4NO_3 during the transport process from China to Fukuoka. The temporal behaviors of gas-phase HNO_3 and NH_3 were similar for type N; however, the NH_3 concentration was lower. adjGR showed almost NH_3-neutral conditions during type S. The production of SO_4^{2-} and the insufficient supply of NH_3 contributed to the rapid decomposition of NH_4NO_3 in this case.

In this study, we clarified the two types transport pattern for SNA. The spatial distribution pattern of the outflow over East Asia during January 2015 showed that the outflow of SO_4^{2-} stretched over the whole of western Japan, whereas the transboundary air pollution of NO_3^- played an important role over Kyushu Island, western Japan. Generally, the transboundary air pollution dominated by SO_4^{2-} (type S) has been recognized over East Asia, but we have elucidated the effect of the transboundary heavy pollution dominated by NO_3^- (type N). Our findings will promote the importance of NO_3^- long-range transport.

The study period was limited to January 2015, so the analyzed period should be extended to investigate the type S and N transport patterns further. The variation of the gas ratio for emissions (GRe), which considers the balance between SO_2, NOx, and NH_3 (analogous to Eq. 4) may be useful for future analysis. The emission reductions achieved by the 12th Chinese Five Year Plan during 2011–2015 (Asia Society, 2016), resulted in a GRe increase, which caused an NH_3-rich status compared with the current status. Moreover, the target for the 13th Chinese Five Year Plan during 2016–2020, suggests there will be further increases in GRe. The effects of different reduction rates for SNA precursor gases on transboundary air pollution of NO_3^-, especially over western Japan, should be modeled.

Author contributions

I. Uno designed the synergetic observations at Chikushi Campus of Kyushu University and other remote sites in western Japan. S. Yamamoto and K. Osada respectively carried out the ground-based ACSA and NHx-monitor observations at Fukuoka. Y. Kamiguchi and K. Osada conducted air sampling and chemical analysis for D-F pack samples during the

intensive observation period at Fukuoka. K. Osada and Y. Kurosaki measured $PM_{2.5}$ and analyzed samples at Tottori. K. Tamura analyzed the observations from the remote sites of Tsushima Island and the Goto Islands. Y. Kanaya conducted the BC observations at Fukuoka and the Goto Islands. Z. Wang and S. Itahashi discussed the modeling configuration, and Z. Wang conducted the model comparison to brush up the model results. S. Itahashi developed the modeling system, performed the model simulations and analysis, and prepared the manuscript with contributions from all co-authors.

Acknowledgements

This work was supported by Japan Society for the Promotion of Science (JSPS) KAKENHI Grant Numbers JP25220101, JP23310004, JP15H02803. This work was also supported by the Environment Research and Technology Development Fund of the Ministry of the Environment, Japan (No. S-7, 2-1403, 5-1505). This work was partly funded by the Joint Research Program of Arid Land Research Center, Tottori University (No. 28C2011) and by the Collaborative Research Program of Research Institute for Applied Mechanics, Kyushu University (No. 26AO-2, 27AO-6, 28AO-2). We thank Dr. Sayako Ueda at Nagoya University for analyzing tape filters at Tottori University. We acknowledged the Ministry of the Environment, Japan, which provided preliminary observation data at Tsushima before final production.

References

Ansari, A. S., Pandis, S. N.: response of inorganic PM to precursor conventrations, Environ. Sci. Technol, 32, 2706-2714, 1998.

5   Asia Society: https://www.chinafile.com/reporting-opinion/environment/how-chinas-13th-five-year-plan-addresses-energy-and-environment. last access: 1 September 2016

Appel, B. R., Tokiwa, Y., Haik, M.: Sampling of Nitrates in Ambient Air. Atmos. Environ., 15, 283-289, 1981.

Boylan, J. W., Russell, A. G.: PM and light extinction model performance metrics, goals, and criteria for three-dimensional air quality models, Atmos. Environ., 40, 4946-4959, 2006.

10   Chang, M. C., Sioutas, C., Kim, S., Gong, H. Jr, Linh, W. S.: Reduction of nitrate losses from filter and impactor samplers by means of concentration enrichment, Atmos. Environ., 34, 85-98, 2000.

Carmichael, G. R., Calori, G., Hayami, H., Uno, I., Cho, S. Y., Engardt, M., Kim, S.-B., Ichikawa, Y., Ikeda, Y., Woo, J.-H., Ueda, H., Amann, M.: The MICS-Asia study: model intercomparison of long-range transport and sulfur deposition in East Asia, Atmos. Environ., 36, 175-199, 2002.

15   Carmichael, G. R., Sakurai, T., Streets, D., Hozumi, Y., Ueda, H., Park, S. U., Fung, C., Han, Z., Kajino, M., Engardt, M., Bennet, C., Hayami, H., Sartelet, K., Holloway, T., Wang, Z., Kannari, A., Fu, J., Matsuda, K., Thongboonchoo, N., Amann, M: MICS-Asia II: The model intercomparison study for Asia Phase II methodology and overview of findings, Atmos. Environ., 42, 3468-3490, 2008.

Genfa, Z., Dasgupta, P.K., Dong, S.: Measurement of Atmospheric Ammonia. Environ. Sci. Technol., 23, 1467–1474, 1989.

20   Guenther, A. B., Jiang, X., Heald, C. L., Sakulyanontvittaya, T., Duhl, T., Emmons, L. K., Wang, X: The Model of Emissions of Gases and Aerosols from Nature version 2.1 (MEGAN2.1): an extended and updated framework for modeling biogenic emissions, Geosci. Model Dev., 5, 1471–1492, 2012.

Japan Meteorological Agency: http://www.data.jma.go.jp/svd/vois/data/tokyo/volcano.html. [in Japanese] last access: 14 January 2016

25   John,W., Hering, S., Reischl, G., Sasaki, G., Goren, S.: Characteristics of Nuclepore Filters with Large pore size-II. Filtration Properties, Atmos. Environ., 17, 373-382, 1983.

Ikeda, K., Yamaji, K., Kanaya, Y., Taketani, F., Pan, X., Komazaki, Y. Kurokawa, J., Ohara, T.: Sensitivity analysis of source regions to $PM_{2.5}$ concentration at Fukue island, Japan, J. of the Air & Waste Management Assoc., 64, 445-452, 2014.

30   Itahashi, S., Yumimoto, K., Uno, I., Eguchi, K., Takemura, T., Hara, Y., Shimizu, A., Sugimoto, N., Liu, Z.: Structure of dust and air pollutant outflow over East Asia in the spring, Geosphys. Res. Lett., 37, L20806, doi:10.1029/2010GL044776, 2010.

Itahashi, S., Uno, I., Kim, S-T.: Source contributions of sulfate aerosol over East Asia estimated by CMAQ-DDM, Environ. Sci. Technol, 46, 6733-6741, 2012.

Itahashi, S., Uno, I., Kim, S-T.: Seasonal source contributions of tropospheric ozone over East Asia based on CMAQ-HDDM, Atmos. Environ., 70, 204-217, 2013.

5 Itahashi, S., Uno, I., Hayami, H., Fujita, S: Modeling investigation of controlling factors in the increasing ratio of nitrate to non-seasalt sulfate in precipitation over Japan, Atmos. Environ., 92, 171-177, 2014.

Itahashi, S., Hayami, H., Uno, I.: Comprehensive study of emission source contributions for tropospheric ozone formation over East Asia, J. of Geophys. Res, 120, 331-358, 2015.

Itahashi, S., Hayami, H., Uno, I., Pan, X., Uematsu, M.: Importance of coarse-mode nitrate produced via sea-salt as

10 atmospheric input to East Asian oceans, Geophys. Res, Lett., 43, 5483-5491, 2016.

Itahashi, S., Hayami, H., Yumimoto, K., Uno, I.: Chinese province-scale source apportionments for sulfate aerosol evaluated by the tagged tracer method in 2005, Environmental Pollution, 118, 87-97, 2017.

Irie, H., Muto, T., Itahashi, S., Kurokawa, J., Uno, I.: Turnaround of tropospheric nitrogen dioxide pollution trends in China, Japan, and South Korea, SOLA, 12, 170-174, 2016

15 Kajino, M., Sato, K., Inomata, Y., Ueda, H.: Source-receptor relationships of nitrate in Northeast Asia and influence of sea salt on the long-range transport of nitrate, Atmos. Environ., 70, 67-78, 2013.

Kanaya, Y., Taketani, F., Komazaki, Y., Liu, X., Kondo, Y., Sahu, L. K., Irie, H., Takashima, H.: Comparison of black carbon mass concentrations observed by multi-angle absorption photometer (MAAP) and continuous soot-monitoring system (COSMOS) on Fukue island and in Tokyo, Japan, Aerosol Science and Technology, 47, 1-10, 2013.

20 Kanaya, Y., Pan, X. L., Miyakawa, T., Komazaki, Y., Taketani, F., Uno, I., Kondo, Y.: Long-term observations of black carbon mass concentrations at Fukue Island, western Japan, during 2009-2015: Constraining wet removal rates and emission strengths from East Asia, Atmos. Chem. Phys., 16, 10689-10705, 2016.

Kaneyasu, N., Yamamoto, S., Sato, K., Takami, A., Hayashi, M., Hara, K., Kawamoto, K., Okuda, T., Hatakeyama, S.: Impact of long-range transport of aerosols on the $PM_{2.5}$ composition at a major metropolitan area in the northern

25 Kyushu area of Japan, Atmos. Environ., 97, 416-425, 2014.

Kimoto, H., Ueda, A., Tsujimoto, K., Mitani, Y., Toyazaki, Y., and Kimoto, T.: Development of a Continuous Dichotomous Aerosol Chemical Speciation Analyzer, Clean Technology, 23, 49–52, 2013 (in Japanese).

Khoder, M. I.: Atmospheric conversion of sulfur dioxide to particulate sulfate and nitrogen dioxide to particulate and gaseous nitric acid in an urban area, Chemopshere., 49, 675-684, 2002.

30 Kurokawa, J., Ohara, T., Morikawa, T., Hanayama, S., Greet, J-M., Fukui, T., Kawashima, K., Akimoto, H.: Emissions of air pollutants and greenhouse gases over Asian regions during 2000-2008: Regional Emission inventory in ASia (REAS) version 2, Atmos. Chem. Phys, 13, 11019-11058, 2013.

Li, H., Duan, F., He, K., Ma, Y., Kimoto, T., Huang, T.: Size-dependent characterization of atmospheric particles during winter in Beijing, Atmosphere, 7, 36, 2016.

Li, M., Zhang, Q., Kurokawa, J., Woo, J.-H., He, K. B., Lu, Z., Ohara, T., Song, Y., Streets, D. G., Carmichael, G. R., Cheng, Y. F., Hong, C. P., Huo, H., Jiang, X. J., Kang, S. C., Liu, F., Su, H., Zheng, B.: MIX: a mosaic Asian anthropogenic emission inventory for the MICS-Asia and the HTAP projects, Atmos. Chem. Phys., 17, 935-963, 2017.

Ministry of Environment: http://www2.env.go.jp/pm25monitoring/index.html. [in Japanese] last access: 8 November 2016

Morino, Y., Ohara, T., Nishizawa, M.: Atmospheric behavior, deposition, and budget of radioactive materials from the Fukushima Daiichi nuclear power plant in March 2011, Geophys. Res. Lett., 38, L00G11, 2011.

Morino, Y., Nagashima, T., Sugata, S., Sato, K., Tanabe, K., Noguchi, T., Takami, A., Tanimoto, H., Ohara, T.: Verification of chemical transport model for $PM_{2.5}$ chemical composition using simultaneous measurement data over Japan, Aerosol and Air Quality Research, 15, 2009-2023, 2015.

Nagashima, T., Ohara, T., Sudo, K., Akimoto, H.: The relative importance of various source regions on East Asian surface ozone, Atmos. Chem. Phys., 10, 11305-11322, 2010.

Osada, K., Ueda, S., Egashira, T., Takami, A., Kaneyasu, N.: Measurement of gaseous NH_3 and particulate NH_4^+ in the atmosphere by fluorescent detection after continuous air-water droplet sampling, Aerosol and Air Quality Research, 11, 170-178, 2011.

Osada, K., Kamiguchi, Y., Yamamoto, S., Kuwahara, S., Pan, X., Hara, Y., Uno, I.: Comparison of ionic concentrations on size-segregated atmospheric aerosol particles based on a denuder-filter method and a continuous dichotomous Aerosol Chemical Speciation Analyzer (ACSA-12), Earozoru Kenkyu, 31, 205–211, doi: 10.11203/jar.31.205, 2016. (in Japanese with English abstract)

Pan, X. L., Kanaya, Y., Wang, Z. F., Liu, Y., Pochanart, P., Akimoto, H., Sun, Y. L., Dong, H. B., Li, J., Irie, H., Takigawa, M.: Correlation of black carbon aerosol and carbon monoxide in the high-altitude environment of My. Huang in Eastern China, Atmos. Chem. Phys., 11, 9735-9747, 2011.

Pan, X. L., Uno, I., Hara, Y., Osada, K., Yamamoto, K., Wang, Z., Sugimoto, N., Kobayashi, H., Wang, Z. F.: Polarization properties of aerosol particles over western Japan: classification, seasonal variation, and implications for air quality, Atmos. Chem. Phys., 16, 9863-9873, 2016.

Pan, Y., Tian, S., Liu, D., Fang, Y., Zhu, X., Zhang, Q., Zheng, B., Michalski, G., Wang, Y.: Fossil fuel combustion-related emissions dominate atmospheric ammonia sources during severe haze episodes: Evidence from 15N-stable isotope in size-resolved aerosol ammonium, Environ. Sci. Tech., 50, 8049-8056, 2016.

Pandis, S. N., Seinfeld, J. H.: Sensitivity analysis of a chemical mechanism for aqueous-phase atmospheric chemistry, J. of Geophys. Res., 94, D1, 1105-1126, 1989.

Perrino, C., Santis, F. D., Febo, A.: Criteria for the Choice of a Denuder Sampling Technique Devoted to the Measurement of Atmospheric Nitrous and Nitric Acids, Atmos. Environ., 24, 617-626, 1990.

Petzold, A., Schloesser, H., Sheridan, P. J., Arnott, W. P., Ogren, J. A., Virkkula, A: Evaluation of multiangle absorption photometry for measuring aerosol light absorption, Atmos. Sci. Technol., 39, 40-51., 2005.

Pinder, R. W., Dennis, R. L., Bhave, P. V.: Observable indicators of the sensitivity of $PM_{2.5}$ nitrate to emission reductions - Part I: Derivation of the adjusted gas ratio and applicability at regulatory-relevant time scales, Atmos. Environ., 42, 1275-1286, 2008.

San Martini, F. M., Hasenkopf, C. A., Roberts, D. C.: Statistical analysis of $PM_{2.5}$ observations from diplomatic facilities in China, Atmos. Environ., 110, 174-185, 2015.

Schultz, M. G., Heil, A., Hoelzemann, J. J., Spessa, A., Thonicke, K., Goldammer, J. G., Held, A. C., Pereira, J. M. C., van het Bolscher, M.: Global wildland fire emissions from 1960 to 2000, Glob. Biogeo. Cycles, 22, GB2002, 2008.

Seinfeld, J. H. and Pandis, S. N: Atmospheric Chemistry and Physics – From Air Pollution to Climate Change, 2nd edn., John Wiley & Sons., New York, USA, 2006.

Sickles, J. E. II, Hodson, L. L., Vorburger, L. M.: Evaluation of the filter pack for long-duration sampling of ambient air, Atmos. Environ., 33, 2187-2202, 1999.

Shimadera, H, Hayami, H., Chatani, S., Morino, Y., Mori, Y., Morikawa, T., Yamaji, K., Ohara, T.: Sensitivity analyses of factors influencing CMAQ performance for fine particulate nitrate, J. of the Air & Waste Manage. Assoc., 64 (4), 374-387, 2014.

Skamarock, W. C., Klemp, J. B., Dudhia, J., Gill, D. D., Barker, D. M., Duda, M. G., Huang, X-Y., Wang, W., Powers, J. G.: A description of the advanced research WRF version 3, NCAR Tech. Note, NCAR/TN-475+STR, 113 pp., Natl. Cent. for Atmos. Res., Boulder, Colorado, USA, 2008.

Stein, A. F., Draxler, R. R., Rolph, G. D., Stunder, B. J. B., Cohen, M. D., Ngan, F: NOAA's HYSPLIT atmospheric transport and dispersion modeling system, Bull. Amer. Meteor. Soc., 96, 2059-2077, 2015.

Streets, D. G., Bond, T. C., Carmichael, G. R., Fernandes, S. D., Fu, Q., He, D., Klimont, Z., Nelson, S. M., Tsai, N. Y., Wang, M. Q., Woo, J.-H., Yarber1, K. F.: An inventory of gaseous and primary aerosol emissions in Asia in the year 2000, J. Geophys. Res. Atmos., 2003, 108, doi:10.1029/2002JD003093.

Uno, I., Sugimoto, N., Shimizu, A., Yumimoto, K, Hara, Y., Wang, Z.: Record Heavy $PM_{2.5}$ air pollution over China in January 2013: Vertical and horizontal dimensions, SOLA, 10, 136-140. 2014

Vecchi, R., Valli, G., Fermo, P., D'Alessandro, A., Piazzalunga, A., Bernardoni, V.: Organic and Inorganic Sampling Artefacts Assessment. Atmos. Environ., 43, 1713-1720, 2009.

Wang, H., Tan, S. C., Wang, Y., Jiang, C., Shi, G-Y., Zhang, M-X., Che, H-Z.: A multisource observation study of the severe prolonged regional haze episode over eastern China in January 2013, Atmos. Environ., 89, 807-815, 2014.

Xia, Y., Zhao, Y., Nielsen, C. P.: Benefits of China's efforts in gaseous pollutant control indicated by the bottom-up emissions and satellite observations 2000-2014, Atmos. Environ., 136, 43-53, 2016.

Ying, Q., Wu, L., Zhang, H.: Local and inter-regional contributions to $PM_{2.5}$ nitrate and sulfate in China, Atmos. Environ., 94, 582-592, 2014.

Zheng, G. J., Duan, F. K., Su, H., Ma, Y. L., Cheng, Y., Zheng, B., Zhang, Q., Huang, T., Kimoto, T., Chang, D., Poschl, U., Cheng, Y. F., He, K. B.: Exploring the severe winter haze in Beijing: the impact of synoptic weather, regional transport and heterogeneous reactions, Atmos. Chem. Phys., 15, 2669-2983, 2015.

Zhang, M., Gao, L., Ge, C., Xu, Y.: Simulation of nitrate aerosol concentrations over East Asia with the model system RAMS-CMAQ, Tellus, 59B, 372-380, 2007.
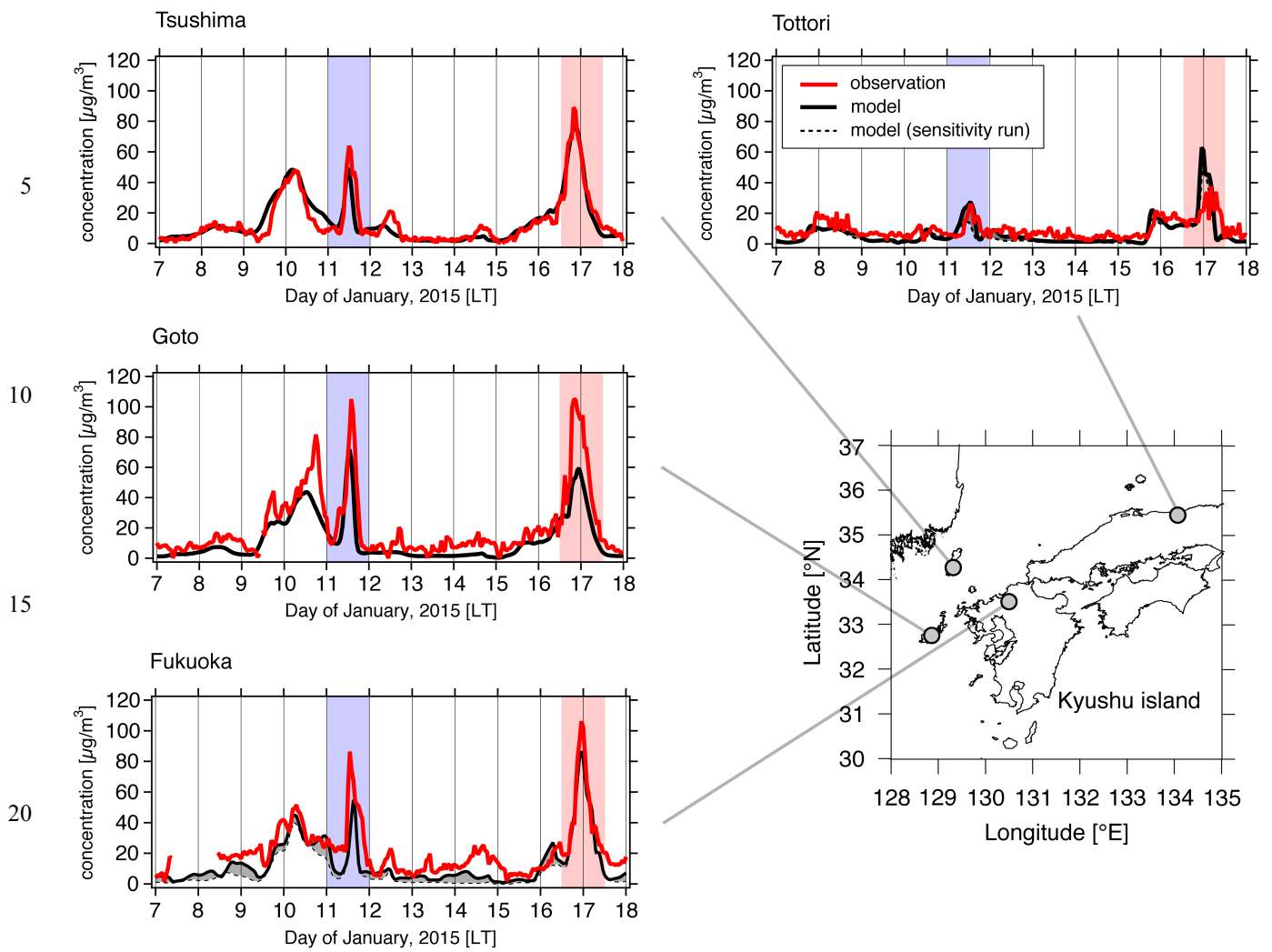
Figure 1: Temporal variation of PM$_{2.5}$ over Japan at Fukuoka, the Goto Islands, Tsushima Island, and Tottori during January 7-17, 2015. Blue and red shading show the episodes focused on in this study. Red lines indicate observations. Black lines indicate the base case simulation and dotted black lines indicate the sensitivity simulation in which the anthropogenic emissions from Japan were switched off; the differences between these results shown in gray represent local contributions.
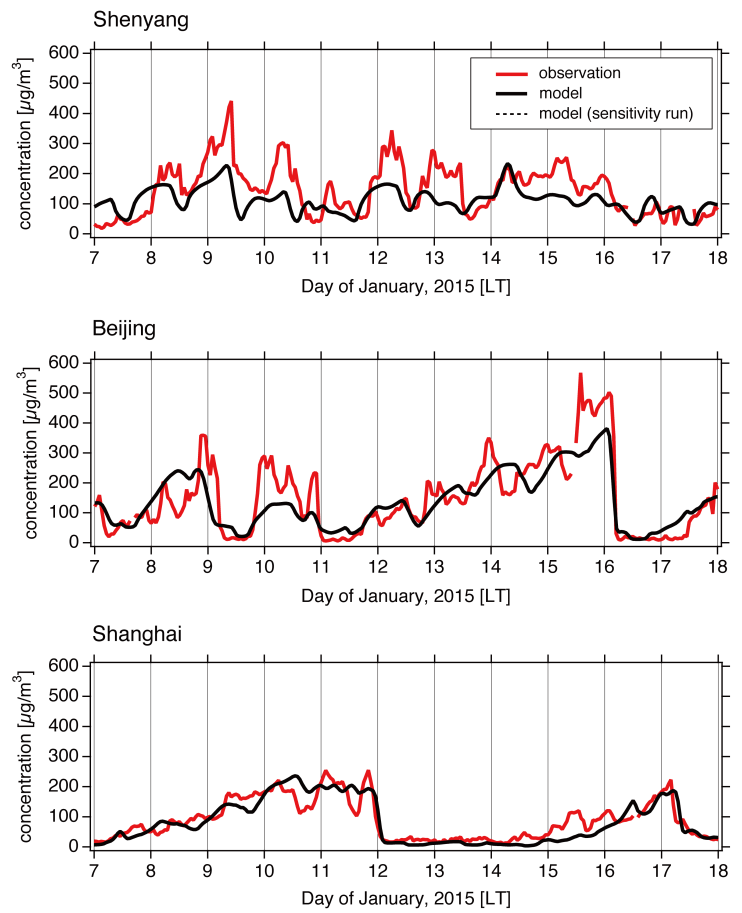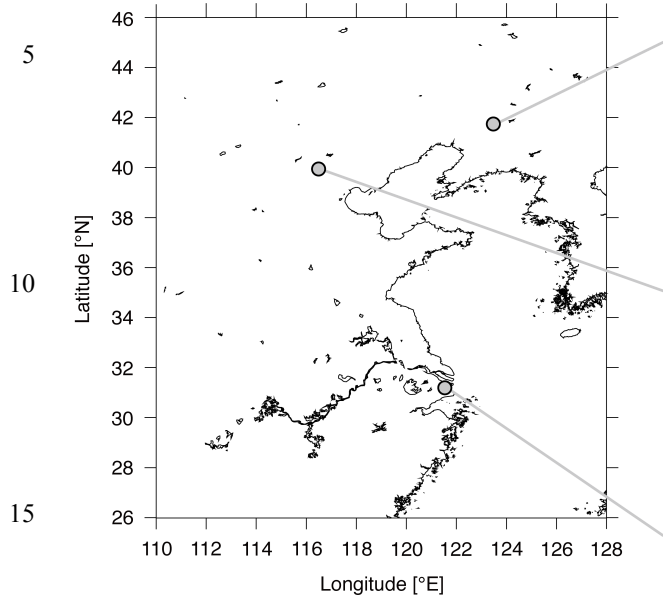
Figure 2: Temporal variation of PM₂.₅ over China at Beijing, Shanghai, and Shenyang during January 7-17, 2015. Red lines indicate observations by BAM at the U.S. Embassy in Beijing and at the U.S. Consulates in Shenyang and Shanghai. Black lines indicate the base case simulation and dotted black lines indicate the sensitivity simulation in which the anthropogenic emissions from Japan were switched off; the differences between these results shown in gray represent Japanese contributions.

anthropogenic NOx emissions [Gg/month]
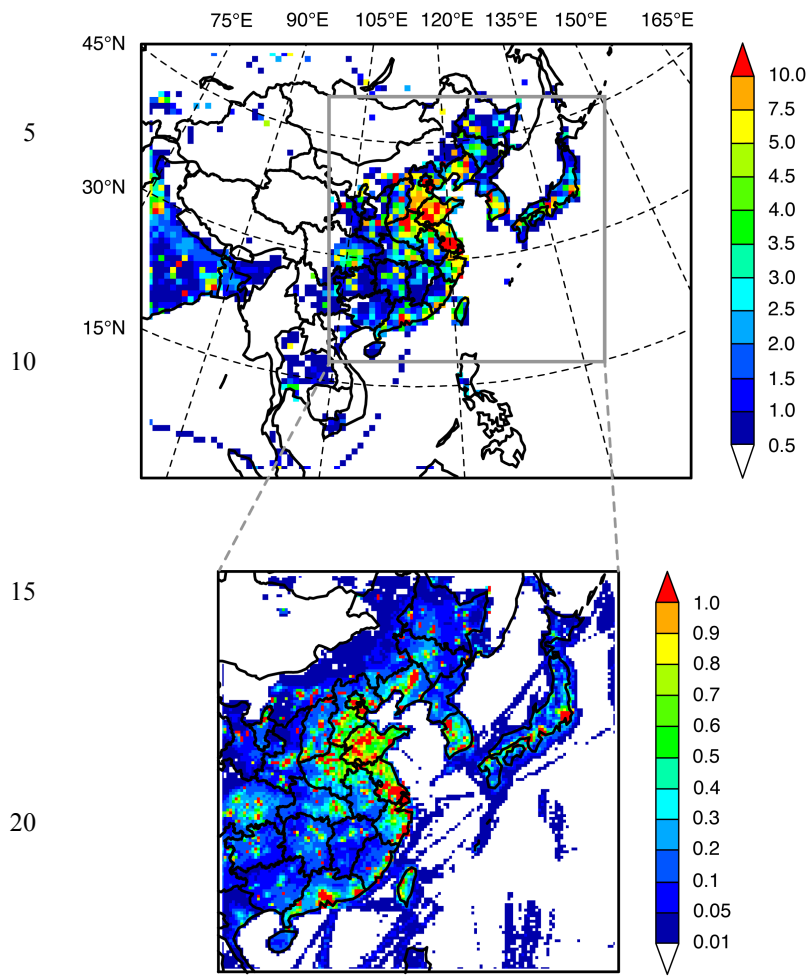
Figure 3: Modeling domain for horizontal resolutions of (top) 81 km and (bottom) 27 km with anthropogenic NOx emissions.
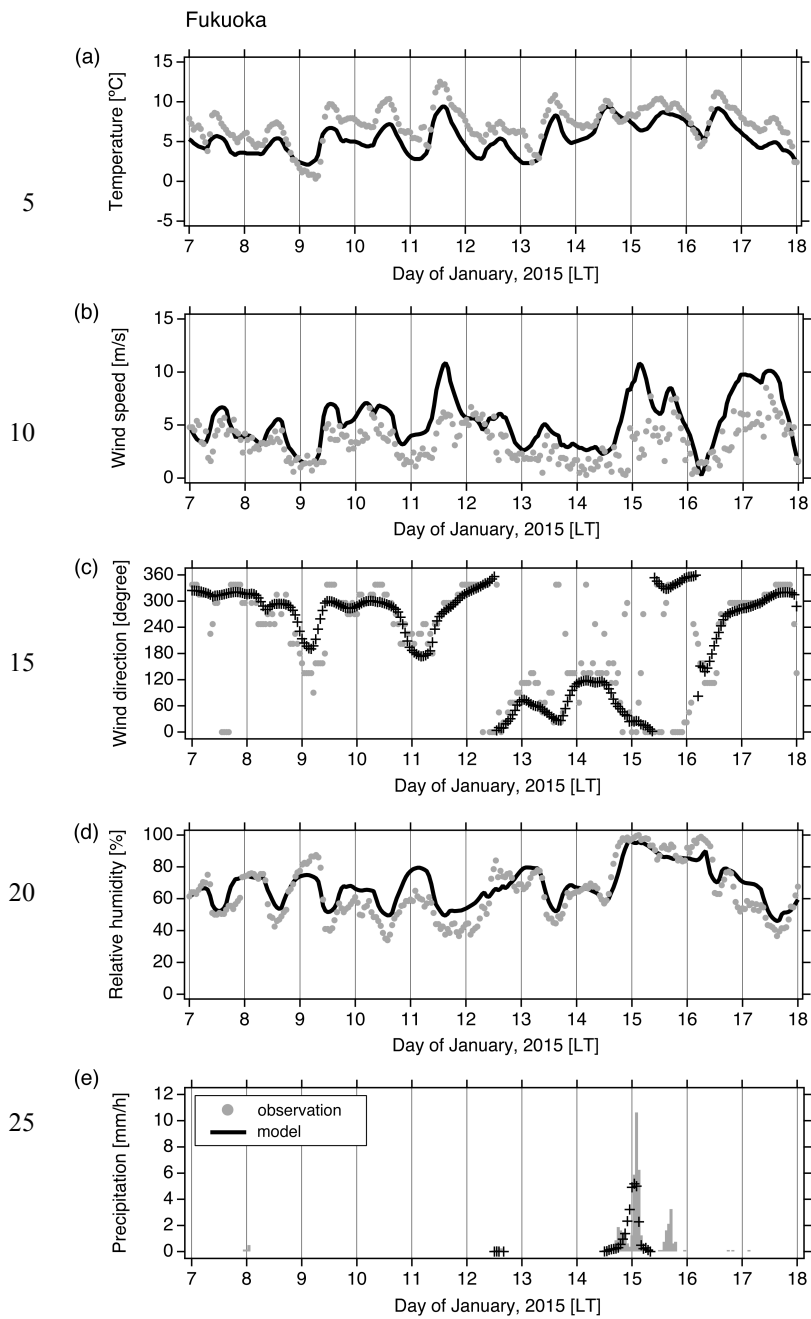
Fukuoka

Figure 4: Temporal variation of (a) temperature, (b) wind speed, (c) wind direction, (d) relative humidity, and (e) precipitation at Fukuoka during January 7-17, 2015. Gray and black indicate observations and model results, respectively.
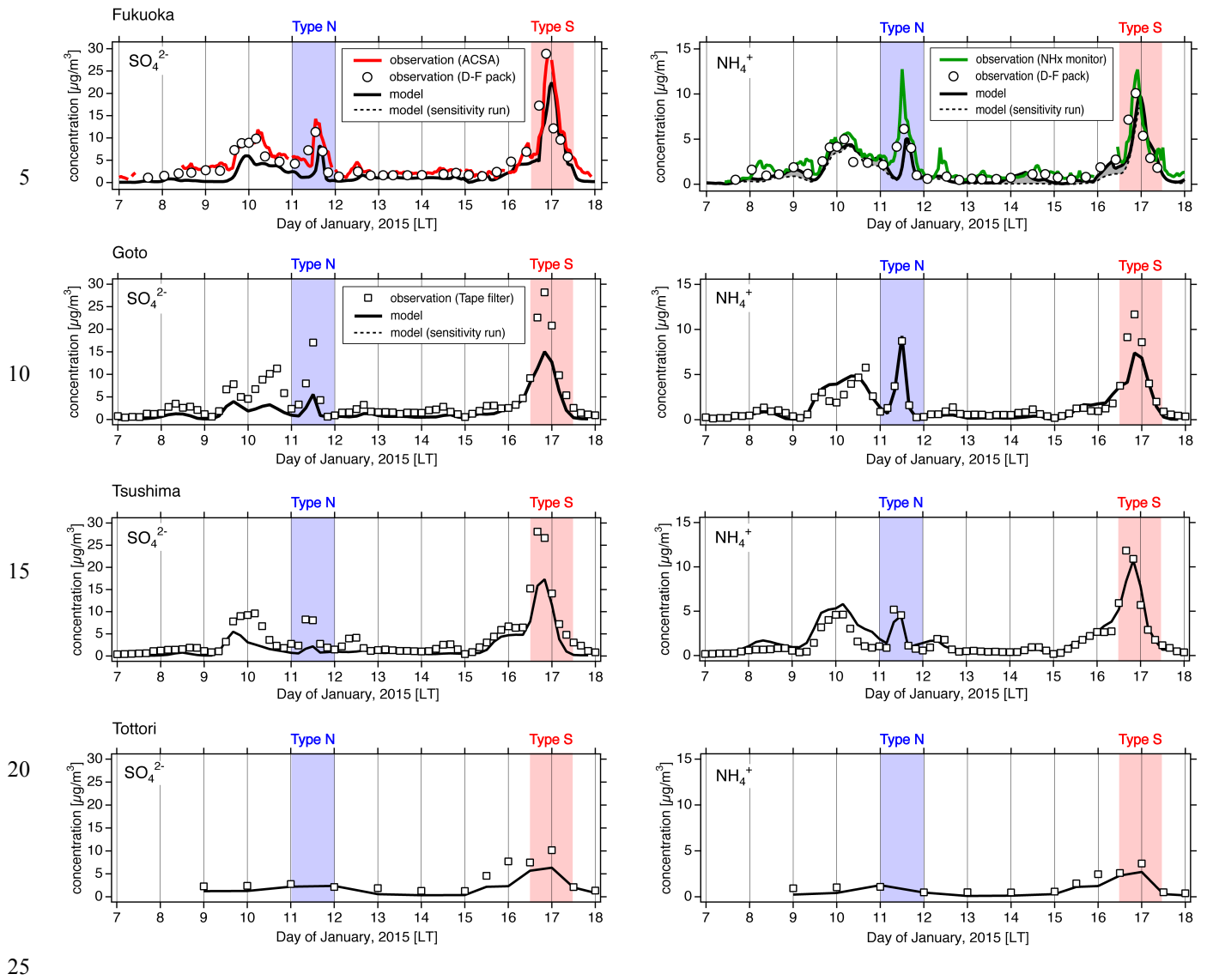
Figure 5: Temporal variation of SO₄²⁻ and NH₄⁺ over Japan at Fukuoka, the Goto Islands, Tsushima Island, and Tottori during January 7-17, 2015. Blue and red shading show the type N and S patterns focused on in this study. Red lines indicate SO₄²⁻ observations by ACSA and green lines indicate NH₄⁺ observations by NHx monitor at Fukuoka. Open circles are D-F pack observations at Fukuoka. Open squares are tape filter measurements at the Goto Islands, Tsushima Island, and Tottori. Black lines indicate the base case simulation and dotted black lines indicate the sensitivity simulation in which the anthropogenic emissions from Japan were switched off; the differences between these results shown in gray represent local contributions.
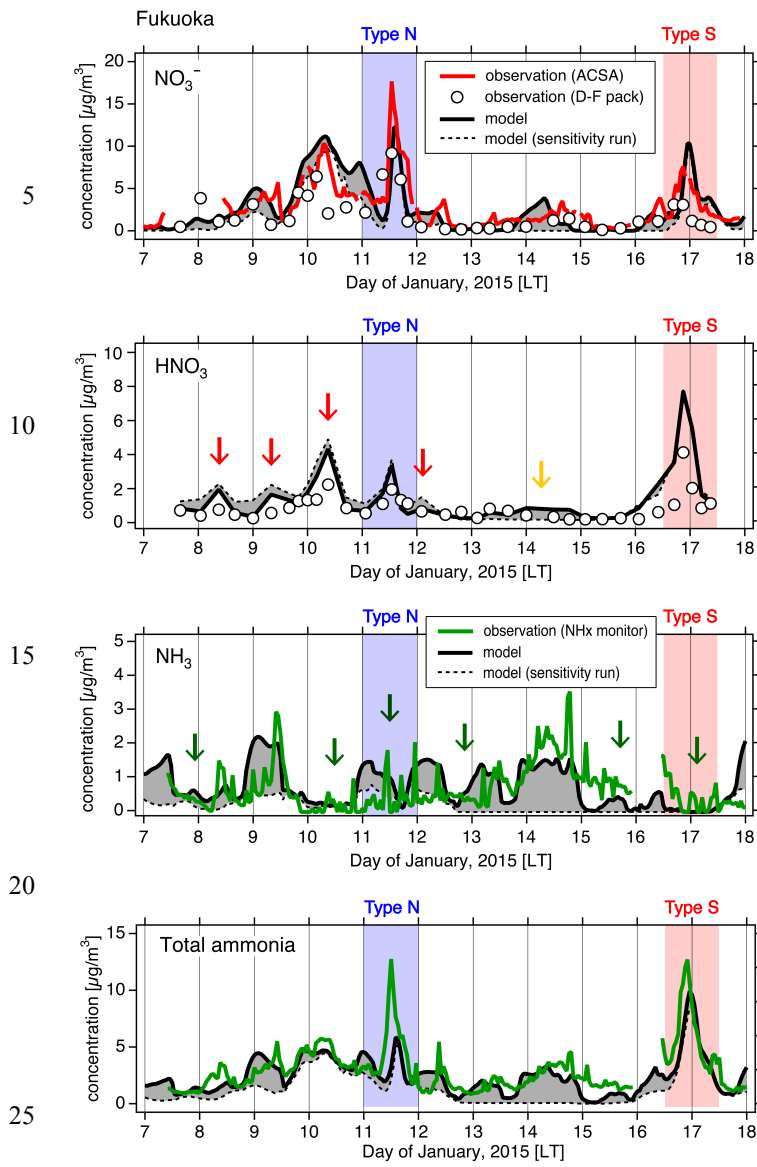
Figure 6: Temporal variation of NO_3^-, HNO_3, NH_3, and total ammonia at Fukuoka during January 7-17, 2015. Blue and red shading show the type N and S patterns focused on in this study. Red lines indicate NO_3^- observations by ACSA, green lines indicate NH_3 and total ammonia observations by NHx monitor, and open circles indicate D-F pack observations. For NH_3, periods of nearly zero concentration (24 h average of less than 1 µg/m^3) are indicated by arrows. Black lines indicate the base case simulation and dotted black lines indicate the sensitivity simulation in which the anthropogenic emissions from Japan were switched off; the differences between these results shown in gray represent local contributions.
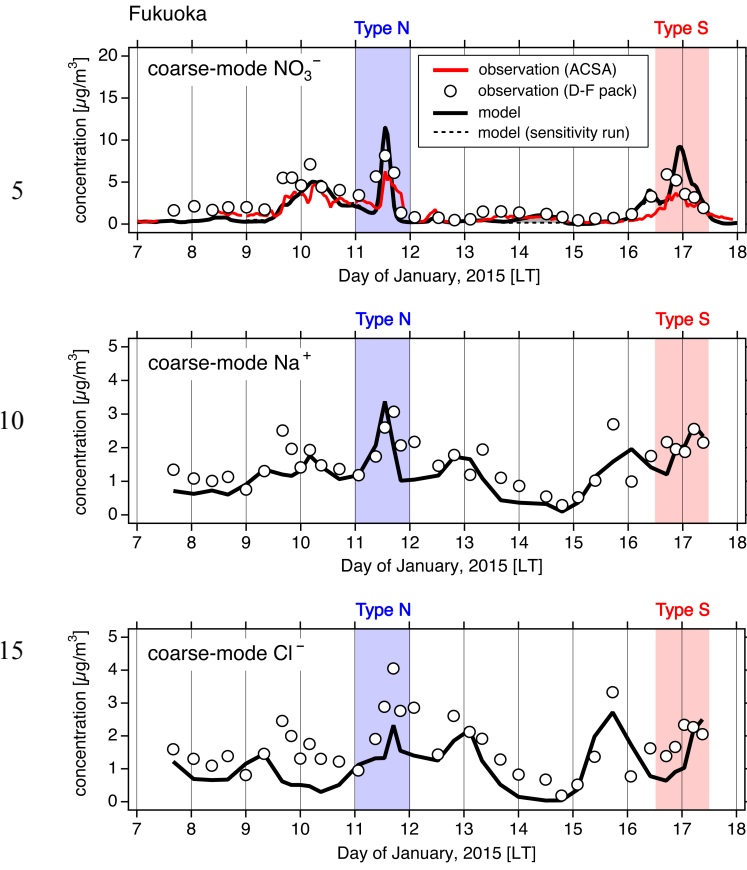
Figure 7: Temporal variation of coarse-mode NO$_3^-$, Na$^+$, and Cl$^-$ at Fukuoka during January 7-17, 2015. Blue and red shading show the type N and S patterns focused on in this study. Red lines indicate coarse-mode NO$_3^-$ observations by ACSA and open circles indicate D-F pack observation. Black lines indicate the base case simulation and dotted black lines indicate the sensitivity simulation in which the anthropogenic emissions from Japan were switched off; the differences between these results shown in gray represent local contributions.
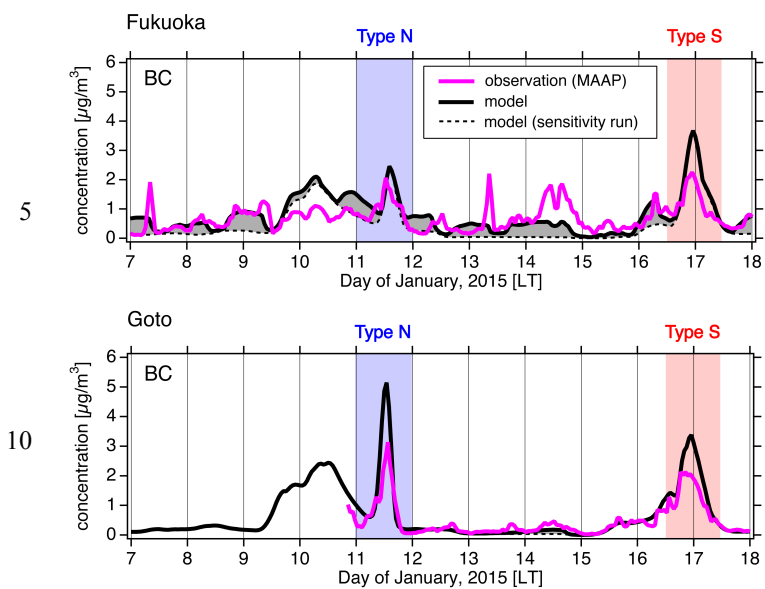
Figure 8: Temporal variation of BC at Fukuoka and the Goto Islands during January 7-17, 2015. Blue and red shading show the type N and S patterns focused on in this study. The magenta line indicates BC observations by MAAP. Black lines indicate the base case simulation and dotted black lines indicate the sensitivity simulation in which the anthropogenic emissions from Japan were switched off; the differences between these results shown in gray represent local contributions.
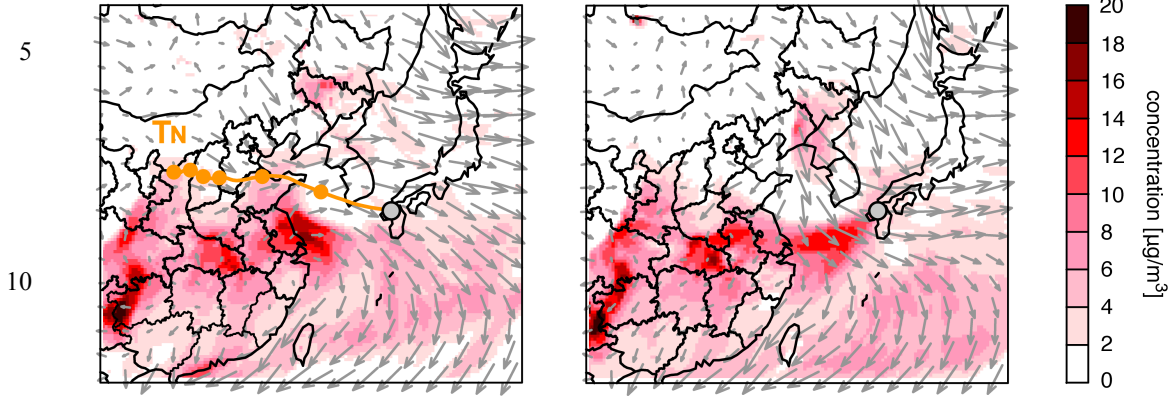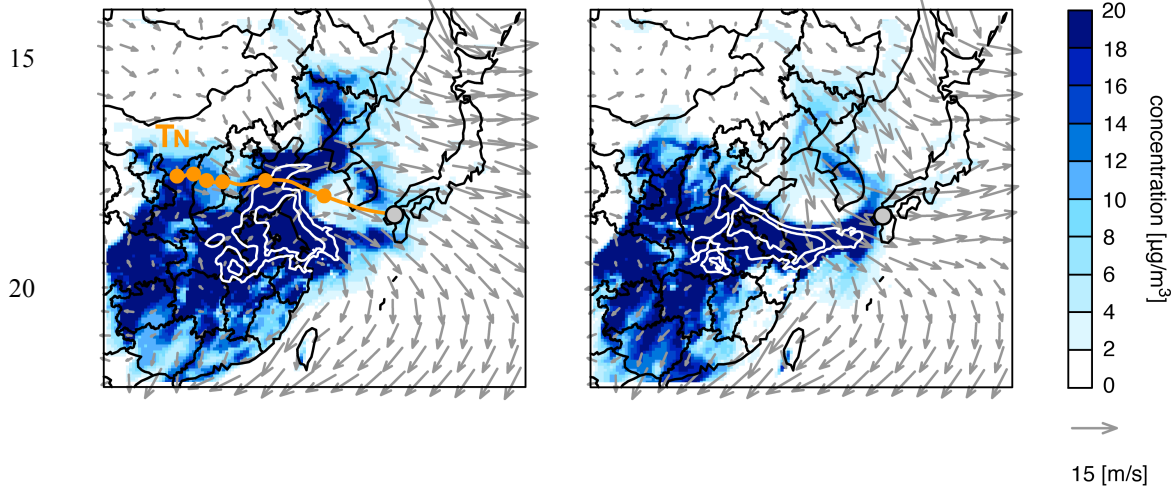
Figure 9: Simulated spatial distribution for (a) SO₄²⁻ and (b) NO₃⁻ during type N pattern. Contours shown by white lines for NO₃⁻ represent 40 and 60 µg/m³. The 72 h HYSPLIT backward trajectory from Fukuoka is overlaid with orange lines with circles at 12 h intervals. (Left) 21:00 LT, January 10, 2015, when the air mass left China, and (right) 15:00 LT, January 11, 2015, when the air mass reached Fukuoka.

Type S

00:00 LT, January 16, 2015   00:00 LT, January 17, 2015

(a) SO₄²⁻
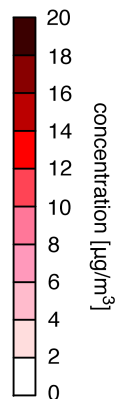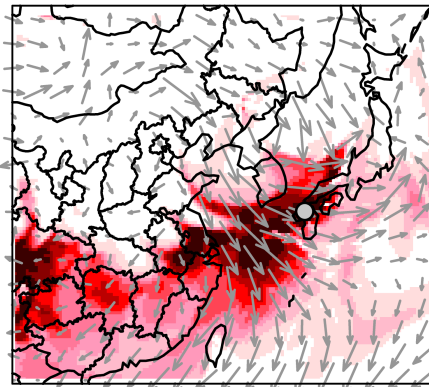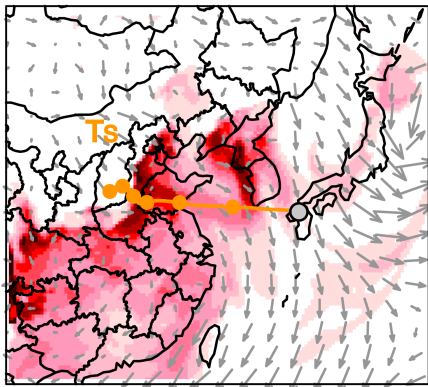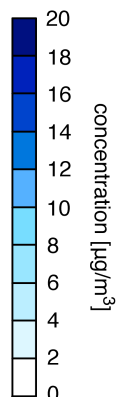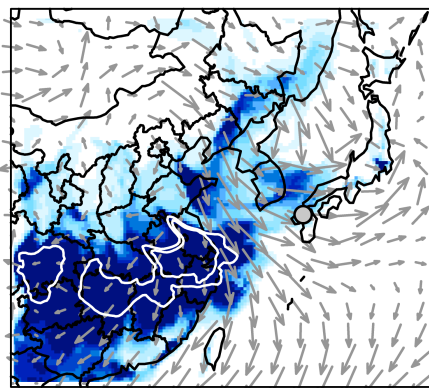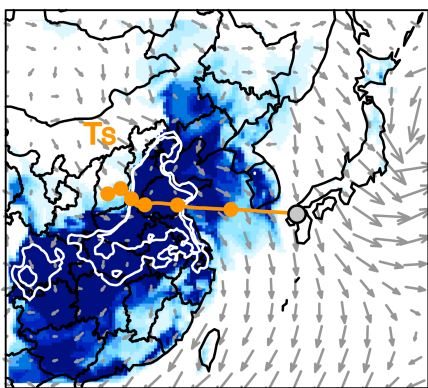
(b) NO₃⁻

15 [m/s]

Figure 10: Simulated spatial distribution for (a) SO₄²⁻ and (b) NO₃⁻ during type S pattern. Contours shown by white lines for NO₃⁻ represent 40 and 60 µg/m³. The 72 h HYSPLIT backward trajectory from Fukuoka is overlaid with orange lines with circles at 12 h intervals. (Left) 00:00 LT, January 16, 2015, when the air mass left China, and (right) 00:00 LT, January 17, 2015, 00LT when the air mass reached Fukuoka.

Path analysis along backward trajectory T_N
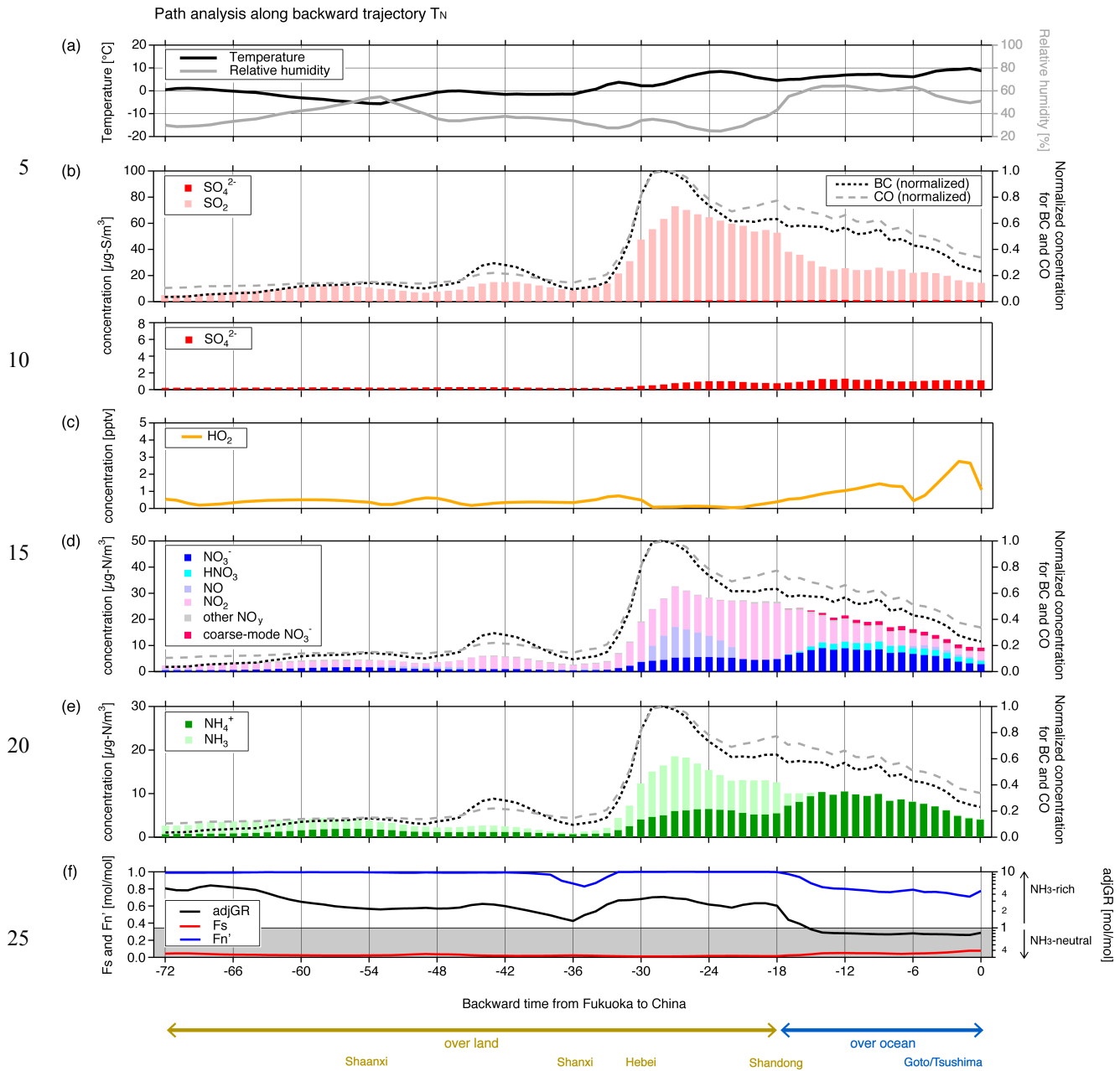
Figure 11: Path analysis of model results along trajectory T_N. (a) Temperature and relative humidity, (b) SO_4^{2-} (with expansion at the bottom) and SO_2, (c) HO_2 concentration, (d) NO_3^-, HNO_3, NO, NO_2, other NOy (NO_3, HNO_2, N_2O_5, and PANs), and coarse-mode NO_3^-, (e) NH_4^+ and NH_3, (f) adjGR, Fs, and Fn'. In (b), (d), and (e), BC and CO concentrations normalized to the maximum value are also shown. Time axis indicates the backward time from Fukuoka. Brown and blue bars at the bottom are schematic images of the trajectory location over land and ocean.
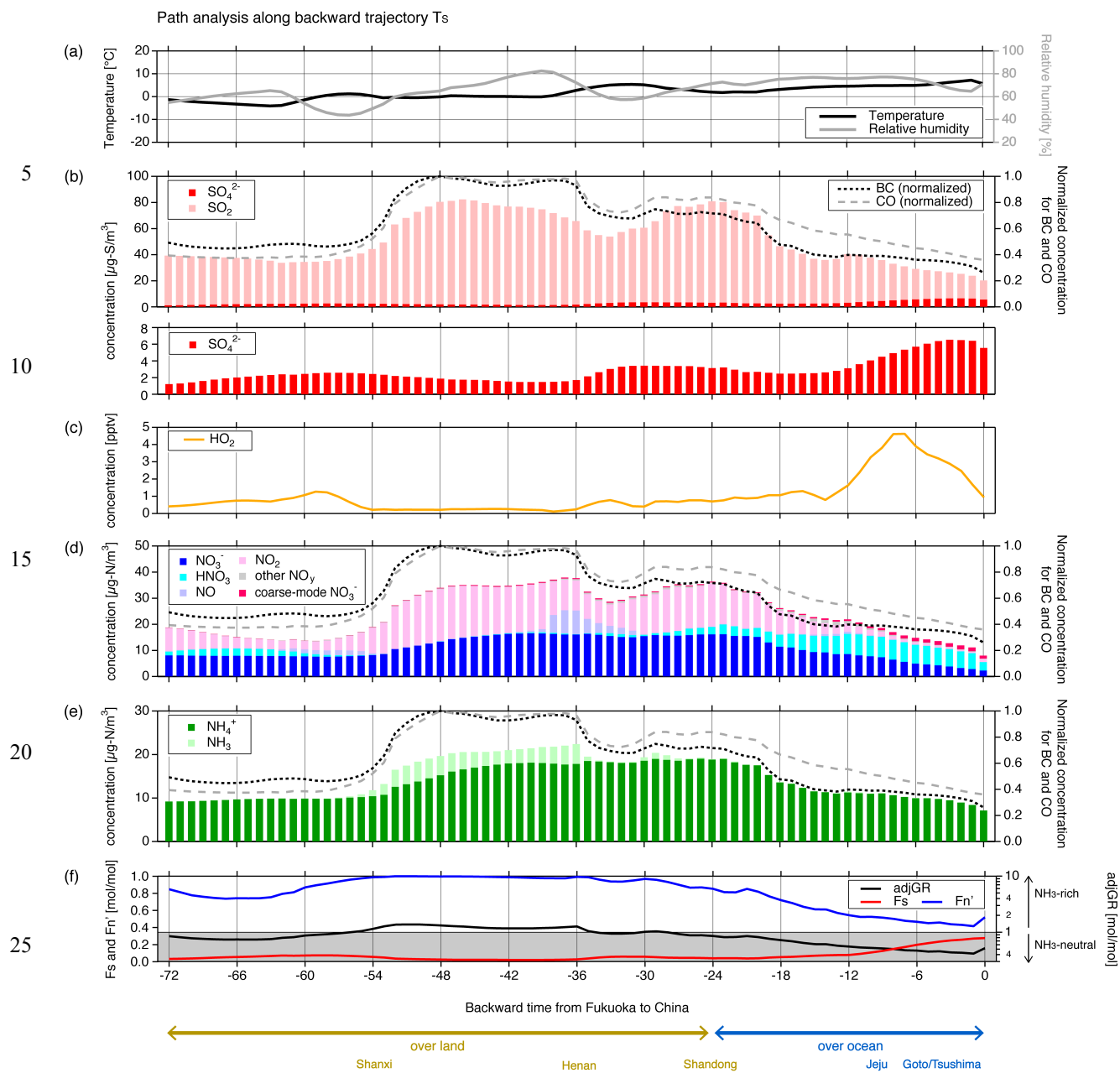
Figure 12: **Path analysis of model results along trajectory T$_S$. (a) Temperature and relative humidity, (b) SO$_4^{2-}$ (with expansion at the bottom) and SO$_2$, (c) HO$_2$ concentration, (d) NO$_3^-$, HNO$_3$, NO, NO$_2$, other NOy (NO$_3$, HNO$_2$, N$_2$O$_5$, and PANs), and coarse-mode NO$_3^-$, (e) NH$_4^+$ and NH$_3$, (f) adjGR, Fs, and Fn'. In (b), (d), and (e), BC and CO concentrations normalized to the maximum value are also shown. Time axis indicates the backward time from Fukuoka. Brown and blue bars at the bottom are schematics of the trajectory location over land and ocean.**

Figure 13: Path analysis of model results along trajectories T_N and T_S. Percentages of each concentration relative to the sum of the SO_4^{2-}, NO_3^-, and HNO_3 concentrations in equivalent units are shown. Time axis indicates the backward time from Fukuoka. Brown and blue bars at the bottom are schematics of the trajectory location over land and ocean.
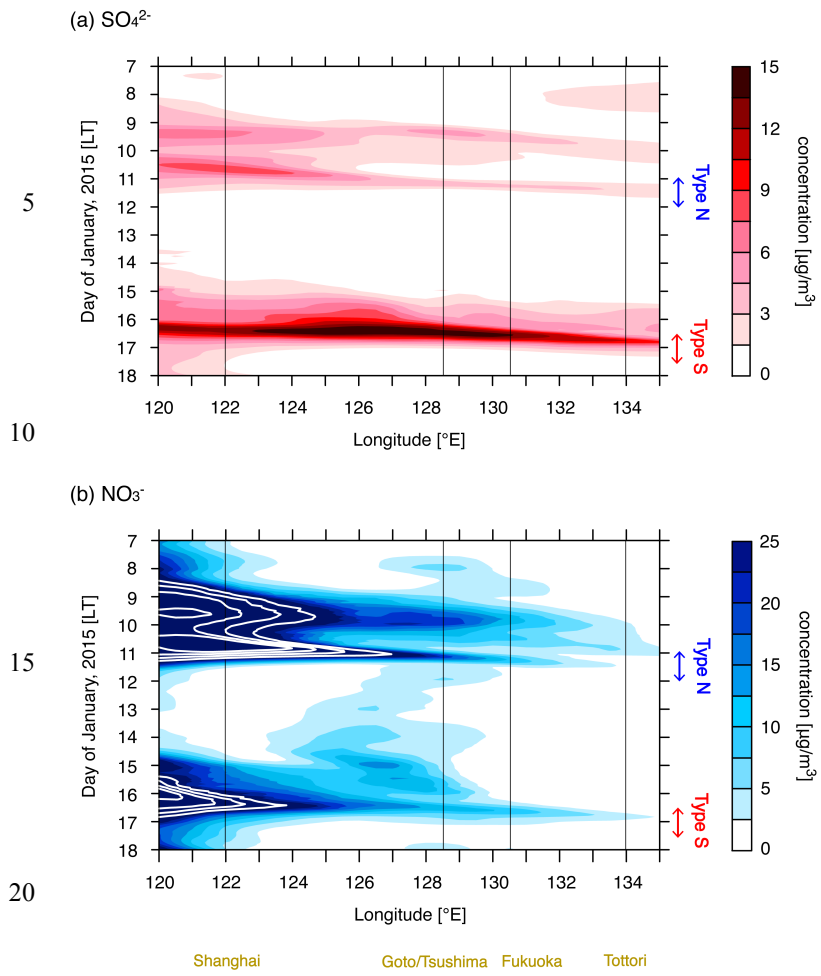
Figure 14: Outflow frequency of (a) SO$_4^{2-}$ and (b) NO$_3^-$. Contours shown by white lines for NO$_3^-$ represent 30, 40, 50, and 60 μg/m^3. Model results are averaged over 32–36°N, and are shown as the time-longitude cross section. Longitudes of representative locations are indicated by thin black lines and the location names are written in brown at the bottom of the figure.

Table 1. Anthropogenic emission amounts used in this study. Units are Gg/month for January 2015.

	China	Republic of Korea	Japan
SO_2	2882.2	35.8	61.1
NO_x	2150.2	90.3	189.3
NH_3	642.1	15.0	15.3

Table 2. Summary of path analysis for types N and S.

Type	Type N			Type S		
Arrival time at Fukuoka	15:00 LT, January 11			00:00 LT, January 17		
Transport time from China	18 h			24 h		
	Over China	During transport	Over Fukuoka	Over China	During transport	Over Fukuoka
Temperature [°C]	6.6	6.7	9.3	3.1	4.0	6.5
Relative humidity [%]	32.7	60.5	50.5	66.3	74.4	67.0
SO_4^{2-} [μg-S/m^3]	0.9	1.1 (+24.5%)	1.1 (+25.5%)	3.3	3.7 (+14.1%)	6.2 (+67.2%)
SO_2 [μg-S/m^3]	55.9	25.0	14.1	72.1	40.0	17.0
Total sulfate [μg-S/m^3]	56.8	26.1 (-54.1%)	15.2 (-74.7%)	75.4	43.8 (-41.9%)	23.1 (-73.2%)
Fs [mol/mol]	0.02	0.04	0.07	0.04	0.10	0.27
NO_3^- [μg-N/m^3]	4.9	7.5 (+53.6%)	3.3 (-42.0%)	15.9	9.4 (-41.1%)	2.8 (-85.6%)
HNO_3 [μg-N/m^3]	0.0	2.1	1.7	1.9	6.1	5.2
Other NOy [μg-N/m^3]	22.2	8.5	3.3	16.7	6.4	0.9
Coarse-mode NO_3^- [μg-N/m^3]	0.0	1.1	1.4	0.4	0.7	1.4
Total NOy [μg-N/m^3]	27.1	19.1 (-29.3%)	9.7 (-66.2%)	34.8	22.5 (-35.3%)	10.4 (-77.0%)
Fn' [mol/mol]	1.00	0.81	0.73	0.90	0.61	0.45
NH_4^+ [μg-N/m^3]	5.6	8.7 (+54.3%)	4.4 (-28.9%)	18.8	12.6 (-33.0%)	8.2 (-62.1%)
NH_3 [μg-N/m^3]	7.5	0.4	0.2	0.6	0.1	0.0
Total ammonia [μg-N/m^3]	13.2	9.1 (-30.7%)	4.6 (-67.9%)	19.5	12.7 (-34.8%)	8.2 (-63.3%)
adjGR [mol/mol]	2.56	0.87	0.77	0.93	0.61	0.46
BC [μg/m^3]	6.5	5.2 (-20.2%)	2.6 (-63.3%)	9.7	6.1 (-37.4%)	4.0 (-63.9%)
CO [ppbv]	904.4	737.6 (-18.4%)	440.2 (-53.8%)	1260.0	887.0 (-29.8%)	564.9 (-56.8%)
Key points	• Dominance of NO_3^- compared with SO_4^{2-} • Under 10% conversion ratio for SO_4^{2-} • Lower relative humidity • Abundant NH_3 supply above China • NH_3-rich air mass maintaining neutralization of NO_3^-			• Dominance of SO_4^{2-} compared with NO_3^- • Approximately 30% conversion ratio for SO_4^{2-} • Higher relative humidity of around 70% • No NH_3 in gas-phase • NH_3-neutral conditions during transport, SO_4^{2-} neutralized		

Note: Parentheses indicate the multiplying factors compared with the status over China. The status is averaged over 6 h before the air mass leaves China, over during transport time from China to Fukuoka above the ocean, and over 3 h before the air mass reaches Fukuoka. Other NOy consists of NO, NO_2, NO_3, HNO_2, N_2O_5, and PANs.